Journal of Marine Research, 44, 227–266, 1986

Journal of
MARINE RESEARCH

Volume 44, Number 2

On the upwelling circulation over the wide shelf off Peru: 2. Vertical velocities, internal mixing and heat balance

by Gary Shaffer[1]

ABSTRACT

An analysis is presented of the mean coastal upwelling circulation over the wide shelf off Peru based on the current and temperature profiling measurements described in Shaffer (1982). The natural coordinate conservation method (NCCM) in temperature (T) space is applied to boxes formed from stations along two lines with 60 km alongshore separation. Mean distributions in x (cross-shelf coordinate) and T are obtained for diapycnal advection and mixing. The vertical component of isopycnal flow is also calculated and found to be considerably less than vertical, diapycnal flow in this region of strong upwelling and internal mixing.

Richardson numbers (Ri) are also studied as an independent way of looking at the internal mixing. Both the x-T distributions of Ri statistics and of "mean" Ri calculated as the ratio of the mean square bouyancy frequency to the mean square current shear show similar structure. Both the results for Ri and K (the coefficient of diapycnal turbulent diffusion of heat) from the NCCM calculation indicate strongest internal mixing and upwelling at the base of an inclined frontal zone.

General $K(Ri)$ relationships are discussed and a particular form is chosen and "calibrated" with the mean Ri and mean K results from a number of common bins in x-T space. The "best choice" $K(Ri)$ is then used to calculate new, "improved" distributions of the diapycnal exchanges. Maximum values for K and upwelling at the base of the frontal layer are ~ 5 cm^2 s^{-1} and $\sim 7 \times 10^{-3}$ cm s^{-1}. A procedure is described for calculating mean upwelling circulation from known distributions of diapycnal exchanges. As expected, the circulation based on the diapycnal exchanges from the $K(Ri)$ model agrees best with observed current structure, calculated Ekman transport in the surface layer and heat balance requirements. The heat balance calculation indicated that shoreward eddy heat flux supplies more heat to the nearshore surface layers of northern Peru than direct surface heating.

It is concluded that the $K(Ri)$ results obtained here may have a certain universal character and

1. Oceanographic Institute, University of Gothenburg, Box 4038, S-400-40 Gothenburg, Sweden.

one of the best ways to accurately estimate coastal upwelling circulation may be to observe the Richardson number.

1. Introduction

Observational and theoretical studies of coastal upwelling experienced an upswing during the 1970's. Extensive field experiments—among the largest to date dedicated to deciphering the physical dynamics near a coast—were carried out in particular off Oregon, northwestern Africa and Peru (Smith, 1974; Barton *et al.*, 1977; Brink *et al.*, 1980). These and the other classical coastal upwelling regions—southwestern Africa and the Somali and southern Arabian peninsula during the southwest Monsoon—are characterized by the persistence of cool, nutrient-rich water in the surface layer near the coast with great biological production as a consequence. In the context of this signature it is appropriate to identify the coastal upwelling circulation as the diabatic, nonreversible flow which leads to the "permanent" transformation of subsurface water to surface layer water under the action of persistent coast-parallel winds driving seaward Ekman transport in the surface layer. Such a definition is in the spirit of the pre-1970 one by Smith (1968). As discussed below two essential ingredients in this transformation are surface heating and turbulent mixing.

Perhaps the main thrust of the analyses of the data from the field studies cited above has been toward essentially adiabatic, reversible features of the motions observed. In particular coastal-trapped waves have been identified as energetic modes of low frequency variability in these areas, (eg. Kundu *et al.*, 1975, Hsieh, 1982; Smith, 1978). By now, however, it has become clear that coastal-trapped waves are a common feature of the coastal zones of the world's oceans and large lakes whether coastal upwelling is or is not present (eg. Csanady, 1976; Mysak, 1980; Shaffer and Djurfeldt, 1983). Although upwelling may be defined as vertical displacements associated with coastal-trapped waves (Gill and Clarke, 1974) it is not clear what relevance such upwelling has for the diabatic, nonreversible coastal upwelling circulation defined above.

The following scenario helps to identify the coastal upwelling problem as I see it: Within a few pendulum hours after an upwelling-favorable wind starts to blow, an Ekman divergence develops near the coast forcing upward motion there. The shoreward compensation flow is barotropic initially (Allen, 1973). As the vertical displacements of the ambient stratification become large, nonlinear effects may lead to initial, adiabatic frontogenesis in the coastal corner (Pedlosky, 1978). A succession of coastal trapped wave modes arrive from the equatorward edge of the wind zone, set up alongshore pressure gradients and modify alongshore current structure (Suginohara and Kitamura, 1984; McCreary and Chao, 1985). Under the effects of seaward Ekman transport, nonlinearity and increasingly important turbulent entrainment into the surface mixed layer, the frontal layer may surface at the coast and start to proceed seaward (De Szoeke and Richman, 1984). Soon however a combination of increasing

vertical shears—at the base of the Ekman layer and near the frontal layer in association with increasing horizontal density gradients—and decreasing vertical density gradients shoreward and at the base of the frontal layer may lead to critical Richardson numbers. Turbulence following the onset of shear instabilities would mix heat downward and support cross-isopycnal flow. As cooler water reaches the surface near the coast the heat flux from the atmosphere increases. Also baroclinic and mixed baroclinic-barotropic type instabilities may grow, feeding on the potential energy associated with the increasing horizontal density gradients. Resulting eddies transport heat shoreward in the near surface layers (Bryden *et al.*, 1980). Net cooling of the surface layers at the eastern ocean boundary would proceed until surface heating and near surface, shoreward eddy heat transport balance advective cooling and "downward", cross-isopycnal diffusive heat transport. The circulation and stratification in this state are the "steady" diabatic coastal upwelling circulation and associated stratification (of course the diabatic coastal upwelling circulation may be quite time-dependent, depending on the variability of the wind for instance, shown in this paper and discussed in Wang and Mooers (1977)). No models of coastal upwelling have as yet been developed which deal properly with the heat balance.

In Shaffer (1982), henceforth refered to as P1, it was demonstrated that the horizontal circulation observed over the inner part of the wide shelf off northern Peru during November-December 1977 was quite strong and steady as reflected for example in the shoreward compensation flow. Since the divergence of the alongshore flow was observed to be small and the temperature field quite stationary, considerable cross-isopycnal flow was implied. Such flow in the presence of significant stratification implies strong, "downward" cross-isopycnal turbulent heat fluxes and together they imply strong heating of the surface layer. Although a description of this diabatic circulation which advects and mixes nutrients, oxygen, phytoplankton, etc. and is responsible for the enormous productivity found in these regions must be a principal concern of coastal upwelling research, experimental determinations of the diapycnal exchanges in upwelling regions are lacking.

In this paper these diabatic aspects of the coastal upwelling problem are addressed in a further analysis of the P1 data set. The relative stability of the observed currents (P) makes it reasonable to consider mass and heat conservation in temperature space for a number of open boxes. Distributions of diapycnal advection are obtained and compared with vertical components of isopycnal advection. Distributions of diapycnal mixing and coefficients of diapycnal turbulent diffusion of heat, K, are also obtained. Internal mixing is also studied through Richardson numbers formed over 5 m vertical intervals. Ri statistics are investigated and mean Ri are formed from mean square buoyancy frequencies and mean square current shears. After a discussion of possible functional forms and suitable averaging schemes, mean K is plotted against mean Ri, both from a set of bins in x(cross-shelf coordinate) $-$ T space. From a "best choice" $K(Ri)$ function, new distributions of diapycnal exchanges are generated. A procedure

for calculating coastal upwelling circulation from these exchanges is outlined. It is shown that the circulation derived from the $K(Ri)$ diapycnal exchange results is more compatible with calculated Ekman transport in the surface layer and heat balance than the circulation derived from the original conservation calculation exchange results. Measurements of Ri may thus serve to determine the mean coastal upwelling circulation.

2. Data and analysis techniques

The data used here as in P1 consist of absolute current and temperature observations from two lines of profiling stations shown in Figure 1. These sections were occupied 5 times each during moderate, persistent upwelling in November–December 1977. Currents were measured at 5 m intervals from the bottom up to about 10 m depth and temperature was recorded continuously with a free-fall thermistor sonde at each station.

The natural coordinate conservation method (NCCM) is used here to calculated diapycnal advection and diffusion from mass and heat conservation in temperature space. The method has proven useful in a number of physical and ecological studies to which the reader is referred for details (Walin, 1977; Shaffer, 1979; Shaffer and Rönner, 1984). Over the wide shelf of northern Peru, density is determined almost completely by temperature.

Consider a region R bounded by (1) the bottom, (2) chosen, open vertical boundaries separating it from the rest of the ocean, (3) isothermal surfaces and (4) the sea surface (if isothermal surfaces considered intersect it within R). The equations for mass (volume) and heat conservation in temperature space in R are

$$G = M - \partial V/\partial t \tag{1}$$

and

$$F = -c_p \int_{T_0}^{T} (M - \partial V/\partial t)\, dT' - (Q) \tag{2}$$

where M is the transport into R under the isosurface ϕ with temperature T; V is the volume under ϕ within R; G is the transport through ϕ out of R; F is the diffusive heat transport through ϕ out of R; Q is the total surface heat flux in R; T_0 is some temperature less than the minimum temperature occurring in R over the period of interest and c_p is the specific heat. All dependent variables are continuous functions of T and time t. In addition we may write

$$w_D = GC^{-1}, \tag{3}$$

$$f = F C^{-1} \tag{4}$$

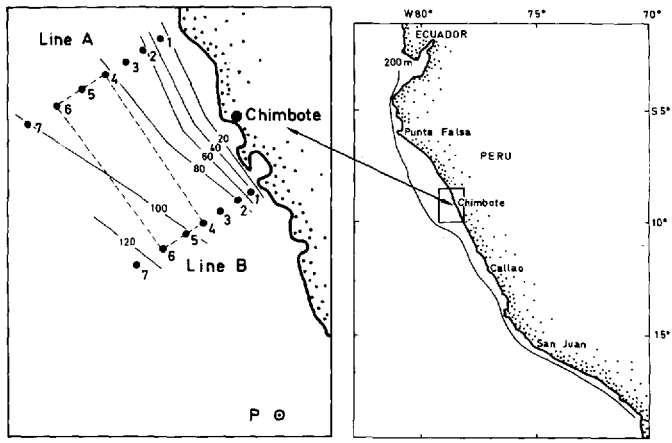

Figure 1. The study area, bottom topography, and locations of stations in lines A and B near 9S from the field experiment during November–December 1977.

and

$$K = (c_p \partial T/\partial \eta)^{-1} f \tag{5}$$

where C is the area of ϕ in R, w_D is the (spatial) mean velocity normal and relative to ϕ in R, f is the mean turbulent heat flux across ϕ in R, and K is the mean coefficient of turbulent heat diffusion defined by relating f to the mean temperature gradient normal to ϕ, $\partial T/\partial \eta$, in the usual manner. Since mean vertical temperature gradients outside of mixed layers are always much greater than mean horizontal ones in the ocean, we identify w_D as the vertical component of flow across isopycnal surfaces and may replace $\partial T/\partial \eta$ by $\partial T/\partial z$ in (5) outside of the mixed layers. From (1) to (5) and for isothermal surfaces below the surface layer

$$K = (C\,\partial T/\partial z)^{-1} \int_{T_0}^{T} C\, w_D dT'. \tag{6}$$

These expressions are applied to the data set described above. Boxes defining the open boundaries of R are formed from short sequences of stations from both lines (see box 6-4 in Fig. 1). For boxes 7-5, 6-4, 5-3, 4-2 and 3-1 daily values of w_D, f and K are calculated for eight days over a ten-day period in steps of .1°C and then averaged over the temperature intervals <14,4°, 14–14,7, 14,7–15,2, 15,2–15,8 and ≥15,8°C. Finally the eight daily values are averaged to form means—$\bar{w}_D$, $\bar{f}$, $\bar{K}$—and standard deviations—σ_{w_D}, σ_f, σ_K, for the study period. The details of this application of the NCCM and motivations for the choices involved are given in Appendix 1.

The vertical component of flow along and with isopycnal surfaces, w_{AD}, may be expressed as

$$w_{AD} = \partial D/\partial t + u\partial D/\partial x + v\partial D/\partial y \tag{7}$$

where $-D(x, y, T, t)$ is the depth to the isotherms at each station and $+u \rightarrow 55°$ and $+v \rightarrow 325°$. For stations 2–6, daily values of w_{AD} are calculated from (7) for the same days and temperature intervals as for w_D (see Appendix 1). Again the eight daily values are averaged to form means, $\overline{w}_{AD}$, and standard deviations, $\sigma_{w_{AD}}$, for the study period.

The Richardson number, Ri, is defined as N^2/S^2 where the buoyancy frequency $N = (g\rho^{-1}\,\partial\rho/\partial z)^{1/2}$ and $S^2 = (\partial u/\partial z)^2 + (\partial v/\partial z)^2$. S^2 is formed from all 5 m separation pairs of individual current observations within the stratified part of the water column. N^2 is calculated from 5 m separation pairs of temperature read off at the depths of the corresponding current observations. A density, ρ, was ascribed to an observed temperature from an empirical $\rho = g(T, S)$ relation based on the data from November 1977 in the study area of Herman (1982) and Doe (1978). Salinity, S, varied by less than .1 ‰ over the water column but had to be included correctly in $g(T, S)$ to avoid unnecessary error in N^2.

3. Vertical velocities

The results for $\overline{w}_D$, the diapycnal "vertical" velocity, and σ_{w_D}, its standard deviation, are listed at their $x - T$ positions in Figure 2a, b. Values are given for each box and temperature range for which w_D could be calculated all eight days. Results of box 7-5 are listed under station 6, etc. The temperature field shown represents the transformation of the alongshore mean of $\mathbf{X}(T)$, the mean locii of T in x, z space for the five sections at each of the two lines. This procedure retains real vertical and horizontal gradients (see P1). Also shown are the mean locii of the surface and bottom mixed layer boundaries.

Figure 2a shows a coherent pattern of $\overline{w}_D$ with the largest upward velocities, $\sim 1.5 \times 10^{-2}$ cm s^{-1}, centered at the base of the frontal layer 15–25 km offshore. Diapycnal velocities decrease considerably both seaward and downward from this maximum. On the other hand the variability of w_D is greatest nearshore where $\sigma_{w_D} \sim 1.4 \times 10^{-2}$ cm s^{-1} (Fig. 2b). $\overline{w}_D$ exceeds σ_{w_D} by about a factor 2 at the base of the frontal layer but σ_{w_D} exceeds $\overline{w}_D$ by that much or more in the nearshore and offshore regions.

The daily variability of $\overline{w}_D$ as expressed by σ_{w_D} may represent real variability associated with changes in the diabatic circulation, uncertainty in the calculations of w_D or a combination of both. Figure 3a shows the time development of the daily values of w_D averaged across all the boxes for the temperature interval 15.2–15.8°C compared to that of the average alongshore wind stress (P1). Whereas w_D appears related to the wind stress during the later part of the study period, this is not so for the first part. This contrasts with the good agreement found in P1 for variations of surface temperature and alongshore and cross-shelf transport at station 5 and suggests that these large variations of w_D are related to uncertainties in the NCCM calculation. This is investigated in more detail in Appendix 2.

Figure 4a, b lists the results for $\overline{w}_{AD}$ and $\sigma_{w_{AD}}$, the mean vertical component of

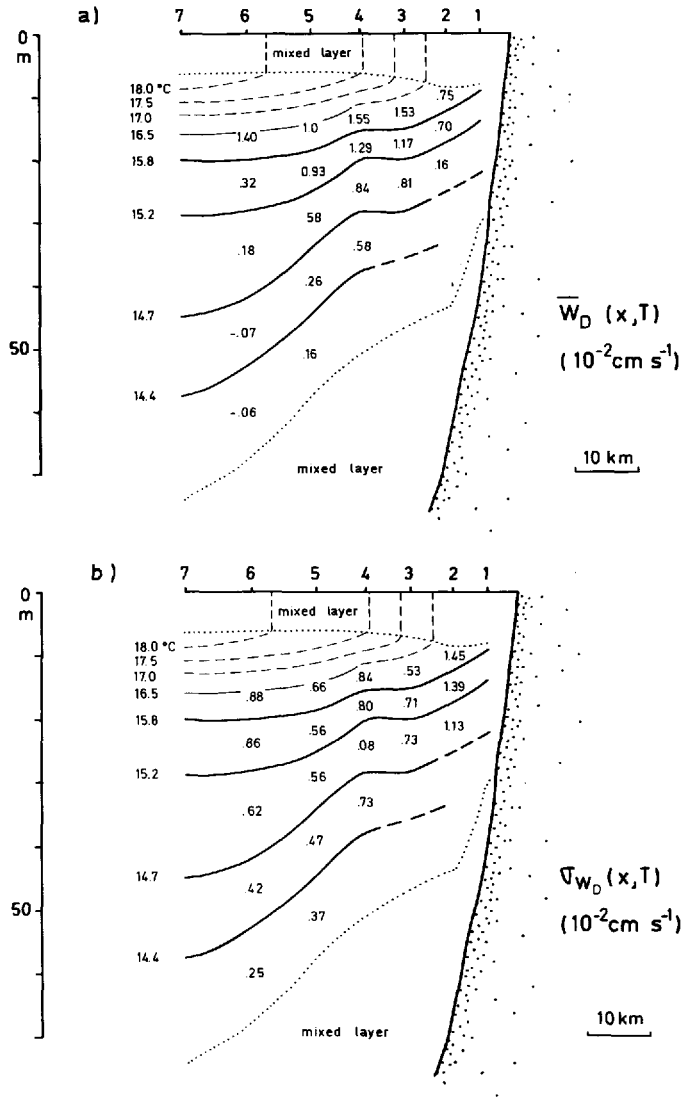

Figure 2. Mean diapycnal "vertical" velocity, $\overline{w}_D$ (a) and its standard deviation σ_{w_D} (b) from the natural coordinate conservation method (NCCM) results listed at their x-T positions. The mean thermal field is averaged between lines A and B.

isopycnal flow and its standard deviation, at their $x - T$ positions. The $\overline{w}_{AD}$ (Fig. 4a) are found to be considerably less than the $\overline{w}_D$ presented above, (Fig. 2a), except at the outer, deeper part of the section where they are comparable. Thus a water parcel flowing into the section at depth with the upwelling compensation current is heated considerably (by heat diffusing downward) before it is upwelled into the surface layer. The variability of w_{AD} is again greatest nearshore where $\sigma_{w_{AD}} \sim .5 \times 10^{-3}$ cm s^{-1} (Fig.

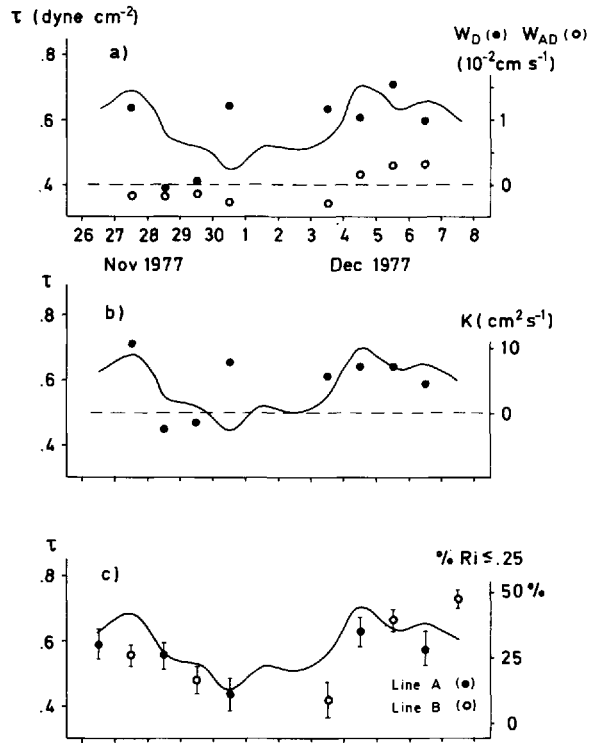

Figure 3. Time development of daily mean diapycnal (w_D) and isopycnal (w_{AD}) vertical velocities (a) and the daily mean coefficient of turbulent heat diffusion, K (b), both for the temperature range 15.2–15.8, and the daily $\%Ri < .25$ statistic (c) compared to the time development of the wind stress.

4b). The time development of w_{AD} averaged across all the boxes for the temperature interval 15.2–15.8°C is also plotted in Figure 3a. It tends to follow the wind, much like the surface temperature in Figure 6a of P1. Indeed the nearshore variability of w_{AD} is real and associated with the vertical isotherm displacements through the $\partial D/\partial t$ terms in (7) following the wind cycle as discussed in P1.

4. Internal mixing

a. Diapycnal turbulent heat fluxes and exchange coefficients. The results for $\bar{f}$, the mean diapycnal turbulent heat flux, and σ_f, its standard deviation are listed in Figure 5a, b at their $x - T$ positions. The $\bar{f}$ (Fig. 5a) are large negative ("downward") near the surface and decrease rapidly in magnitude with depth. Maximum values are found at the base of the frontal layer and strong thermocline, 15–35 km offshore. The σ_f (Fig. 5b) are quite large and have structure similar to $\bar{f}$ except at station 2 and 6 where σ_f is

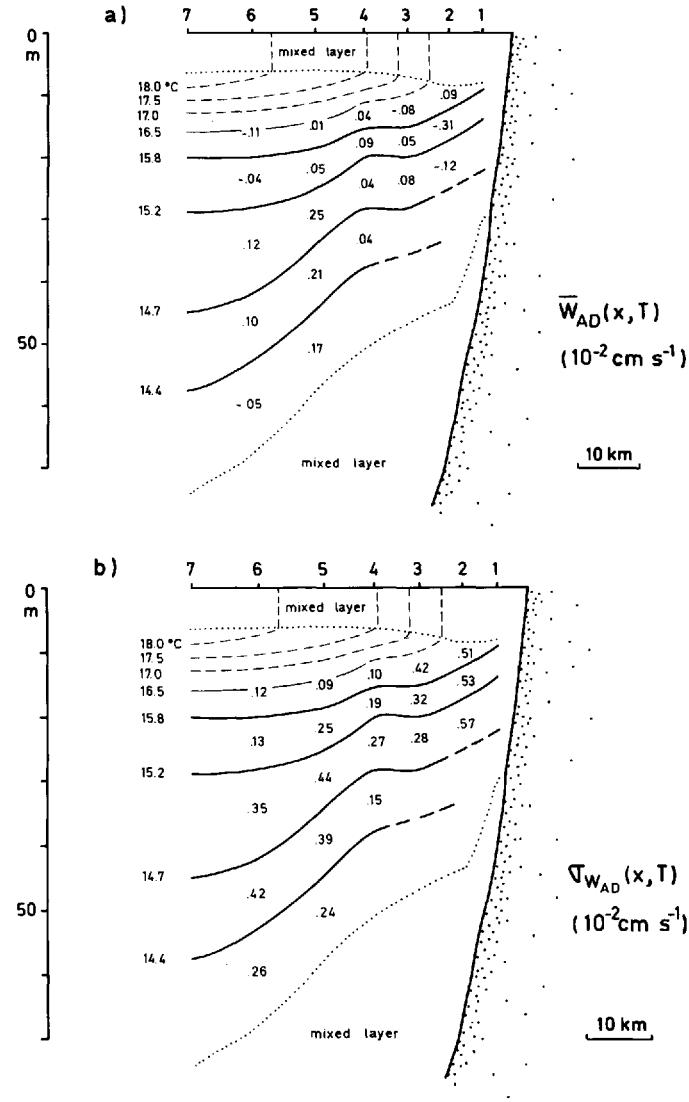

Figure 4. The vertical component of mean isopycnal flow, $\overline{w}_{AD}$ (a) and its standard deviation, $\sigma_{w_{AD}}$, (b) listed at their x-T positions.

largest. Only in a small region at the base of the frontal layer and strong thermocline does $\bar{f}$ exceed σ_f.

The results for $\overline{K}$, the mean coefficient of diapycnal diffusion of heat, and σ_K, its standard deviation, are listed in Figure 6a, b at their $x - T$ positions. The distribution of $\overline{K}$ resembles that of $\overline{w}_D$ as might be expected from (6), constant C and the fact that

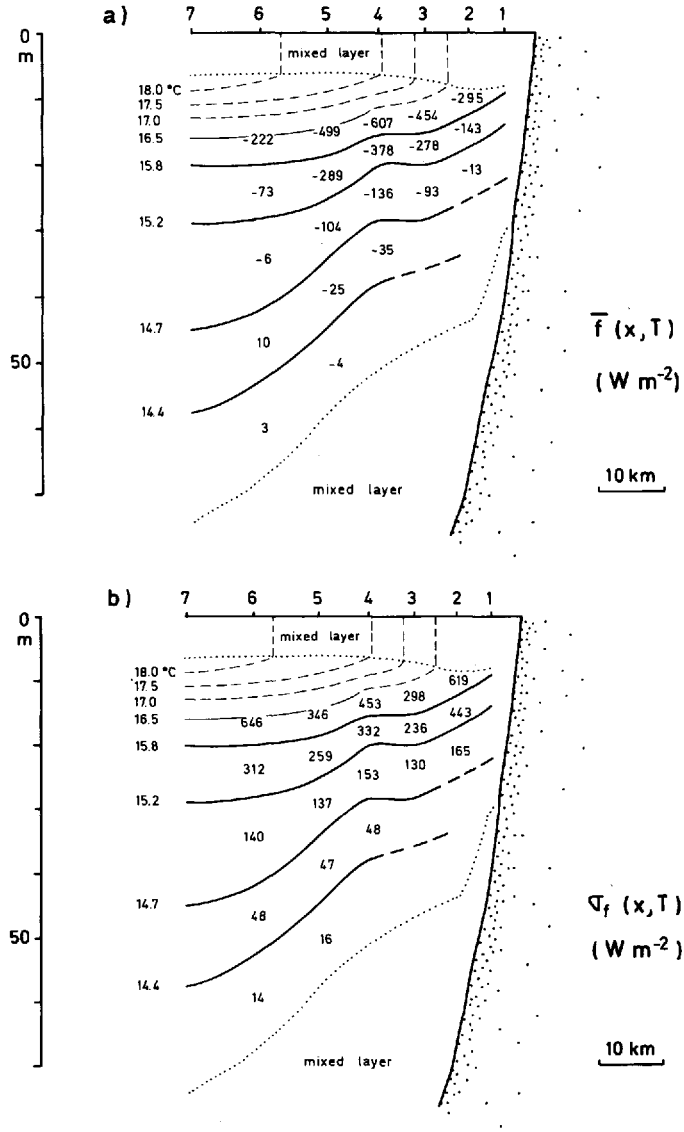

Figure 5. Mean turbulent heat flux, $\bar{f}$ (a) and its standard deviation σ_f (b) from the NCCM calculation listed at their x-T positions.

$\overline{w}_D$ and $\overline{\partial T/\partial z}$ increase monotonically with T. Maximum values of $\overline{K} > 7.0$ cm^2 s^{-1} are found at the base of the frontal layer. Note that $\overline{K}$ appears to be positively correlated with N. $\overline{K}$ exceeds σ_K again only at the base of the frontal layer and increased variability is found at stations 2 and 6.

Figure 3b shows the time development of the daily values of K averaged across all

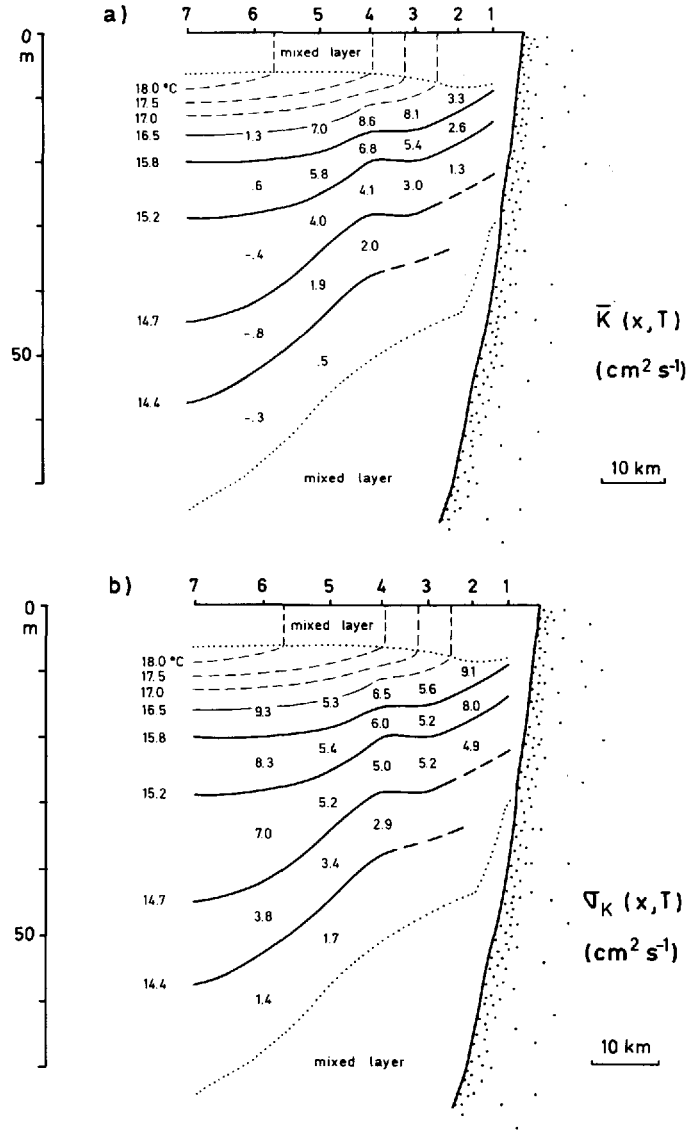

Figure 6. The distribution of mean coefficients of turbulent heat diffusion, $\overline{K}$ (a) and its standard deviation, σ_K (b) from the NCCM calculation listed at their x-T positions.

the boxes for the temperature interval 15.2–15.8° compared to that of the alongshore wind stress. As for w_D, K appears related to the wind stress during the later part of the study period but not during the first part when even improbably negative values are found. It is likely that these initial large variations which contribute greatly to the large standard deviations of $\overline{w}_D$, $\bar{f}$, and $\overline{K}$ are due to the inability of the M calculation to

sufficiently resolve the in and out flows to the boxes all the time (more on this in Appendix 2).

b. Richardson numbers. Laboratory and theoretical studies indicate that low values of *Ri*, the Richardson number, are associated with high levels of turbulence and mixing (eg., Thorpe, 1973). An appropriate vertical scale for calculating *Ri* should be the one which characterizes the largest overturning eddies in the transition from orderly motion to turbulence. A scale commonly chosen to characterize such eddies is the Ozmidov scale, $\lambda = a\,\epsilon^{1/2} N^{-1/2}$ where a is a universal constant near unity and ϵ is the rate of turbulent energy dissipation (Ozmidov, 1965; Thorpe, 1977). The dependence of λ on ϵ and N can be obtained immediately by dimensional analysis under the assumption of a buoyancy subrange. It is an apparent contradiction that a scale depending on the existence of a turbulent subrange, that is a range in wavenumber space which owes its existence to a cascade of energy through it without direct energy input to it, is used to characterize the scale of energy input. Thus λ, which may be identified as the scale at which turbulent motions approach isotropy, is probably a lower bound on appropriate scales for calculating *Ri*.

From the nondivergent, steady state turbulent energy equation we have $K = b\epsilon N^{-2}$ where $b = Rf(1 - Rf)^{-1}$ and Rf is the flux Richardson number, the ratio of rate of removal of energy by buoyancy forces to energy production by vertical shear (eg, Osborn, 1980). Eliminating ϵ we have

$$\lambda = a\, b^{-1/2} K^{1/2} N^{-1/2}. \tag{8}$$

For $a = 1$, $R_f = .1$, observed N^2 and the NCCM K's, we get $\lambda \sim 40$–60 cm in our study region. (With $Rf = .1$, ϵ's ranged from $\sim 3 \times 10^{-3}$ cm^2 s^{-3} at the base of the frontal layer to $< 2 \times 10^{-4}$ cm^2 s^{-3} in the deeper layers offshore.) It would have been more proper to use N^2 calculated over scales closer to λ but, cast in the form of (8), λ is rather insensitive to variations in N^2. From magnitudes of the calculated *Ri*'s and the above discussion our vertical separation scale of 5 m seems to be a reasonable one for calculating *Ri*'s to be compared with the calculated K's.

Figure 7 shows the frequency distribution of the resulting total set of *Ri* for line A ($n = 248$) and line B ($n = 274$) plotted on a log scale. The distributions are quite symmetric and similar with medians of .562 and .586 respectively. The frequency of $Ri \leq .25$ is quite high and also similar, 26.6% and 28.1% for lines A and B respectively implying relatively high levels of turbulence along both lines. A mean Richardson number was also calculated based on the stratification and the square shear averaged over each line. It was found to be somewhat lower for line B than line A, .225 compared to .325. Apparently this is due to the greater frequency of very small *Ri* at line B due to more frequent occurrences of large squared shears, and may imply that turbulence and mixing are somewhat greater along line B. Richardson numbers were also calculated as

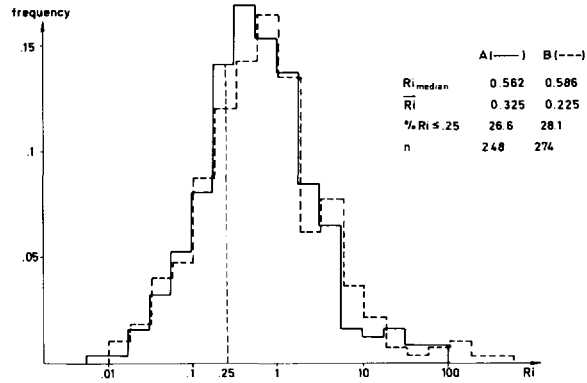

Figure 7. Statistics of instantaneous Richardson number from lines A and B. n is the number individual Ri calculated from each line.

above from the original current and temperature observations but with 10 and 15 m vertical separation, i.e. by skipping over one or two observations when building a current pair. For lines A and B combined, the medians of the resulting distributions increase to 1.38 and 2.01, % $Ri \leq .25$ decrease to 9.9% and 3.9% and mean Ri increase to .625 and 1.094 for $\Delta z = 10$ m and 15 m respectively. These results lend further support to the use of the 5 m separation scale Ri's.

Individual N^2 and S^2 as functions of station number and T—taken as the mean temperature of each data point pair—were collected into bins defined by the somewhat overlapping temperature intervals $\leq$14.45, 14.35–14.75, 14.65–15.3, 15.1–15.9 and $\geq$15.7 and boxes 2–6. The boxes, also overlapping, were formed as for the NCCM calculations above but values of N^2 and S^2 from the central station in each box, eg. station 5 in box 6-4 were given twice the weight of those from the other two stations. The individual N^2 and S^2, typically about 30–40 in each bin, were then averaged to form $\overline{Ri} = \overline{N}^2/\overline{S}^2$ as well as $\overline{Ri}_{max}$ and $\overline{Ri}_{min}$ defined as $\overline{N}^2 + \gamma(\overline{N}^2)/\overline{S}^2 - \gamma(\overline{S}^2)$ and $\overline{N}^2 - \gamma(\overline{N}^2)/\overline{S}^2 + \gamma(\overline{S}^2)$ where γ is the standard error. Preliminary investigation of the individual Ri profiles as well as the pronounced mean vertical current structure exhibited by the data set motivated the choice of the above temperature intervals. Trials with different degrees of overlapping and weighting were made and the above choice appeared to be the best trade off between spacial resolution and accuracy. Also calculations were made with the data from all ten sections and with nine sections excluding A, 1. I chose to concentrate on the latter calculation to avoid bias: A number of important bins were sampled poorly or not at all during A, 1. No major differences emerged between the two calculations however.

Figure 8 shows the distribution of $\overline{Ri}$ calculated as described above. Only the results based on data from all nine sections are included. The general structure of $\overline{Ri}$ is similar to that of $\overline{K}$ (Fig. 6a). Small $\overline{Ri}$ are found at the base of the frontal layer where $\overline{K}$ had its maximum values, the largest $\overline{Ri}$ values are found in the deeper layers offshore as

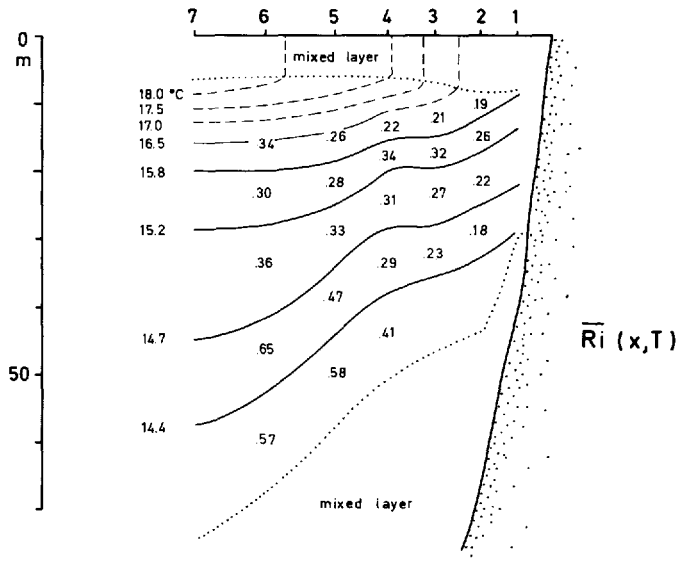

Figure 8. Mean Richardson number, $\overline{Ri}$, listed at their x-T positions.

were the smallest $\overline{K}$ values. A discrepancy does exist however in the deeper layers nearshore where small $\overline{Ri}$ correspond to small to medium values of $\overline{K}$.

An alternative way of investigating the spatial structure of mixing intensity with Ri is to look at the distribution of the statistic % $Ri \leq .25$. Values as small or smaller than this are likely to indicate high levels of turbulence and mixing. Figure 9 shows the number of occasions out of possible nine that a daily Ri calculated by averaging individual N^2 and S^2 for each day and bin fell below .25. There is a good correspondence between the distributions in Figures 8 and 9: more persistent mixing is indicated at the base of the frontal layer and nearshore. This good agreement means that the chances are greater that our $\overline{Ri}$, although based on the relatively few individual N^2 and S^2, is meaningful and representative. Undersampling may not have been a major problem here. In the deeper nearshore layers, however, low $\overline{Ri}$ were not fully reflected in the daily Ri statistics. This imples that a rather limited number of large shear events must have been responsible for low study-period $\overline{Ri}$. This of course is completely possible physically but casts some doubt on the representativity of the $\overline{Ri}$ from those layers.

Finally Figure 3c shows the time development of the statistic % $Ri \leq .25$, based on all individual Ri determinations from each day, compared to the time development of the alongshore wind stress. The values of the statistic were slightly adjusted for bias and the 90% confidence interval is shown (see Appendix 2 for details). The statistic follows the development of the wind remarkably well. The correspondence between lines A and B is also remarkable. The implied daily mean turbulent intensities were moderate at the beginning of the study period, (% $Ri \leq .25 \sim 25\%$) decreased with

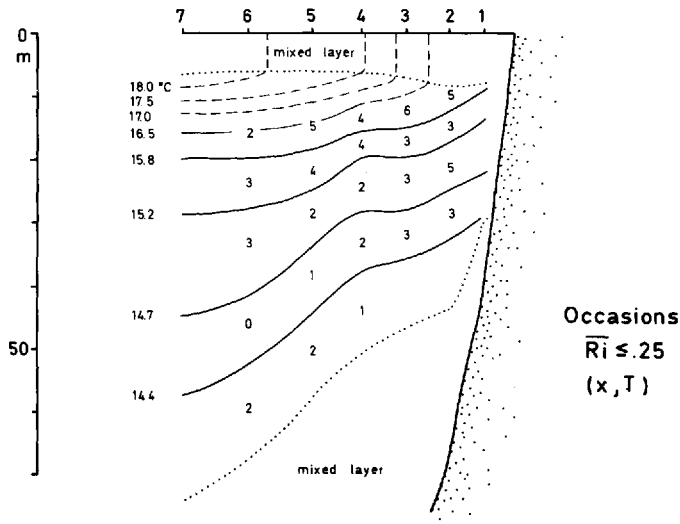

Figure 9. Occasions (of a possible 9) during the study period at which $\%Ri < .25$ listed at their x-T positions.

decreasing wind stress to quite low values (~10%), and increased quite abruptly to high levels (~40%) coincident with a subsequent increase in the wind stress.

c. Relationship of K to Ri. Figure 10 shows $\overline{K}$ plotted as a function of $\overline{Ri}$. The points correspond to values from common x, T positions in Figures 6 and 8. The "error" bars on $\overline{K}$ are $\pm.5\ \sigma_K$. This is a rather arbitrary choice. Five independent boxes can be formed from the five sections along each of line A and B. Were $\overline{K}$ to be calculated from each of these and were the results statistically independent and normally distributed (both of which are probably not true), the standard error of the mean would be $.45\sigma_K$. The ends of the "error" bars on Ri correspond to $\overline{Ri}_{\min}$ and $\overline{Ri}_{\max}$ defined above. Although considerable scatter exists, Figure 10 confirms the impression of Figures 6 and 8 that quite small $\overline{K}$ are found at large $\overline{Ri}$ and $\overline{K}$ tends to increase rapidly as small $\overline{Ri}$ is approached.

The results in Figure 10 suggest that $\overline{K}$ and $\overline{Ri}$ obtained from independent analyses of the same data set are related in a definite manner. Different forms of $K(Ri)$ have been suggested from various theoretical arguments, laboratory and atmospheric data and numerical studies (eg. Munk and Anderson, 1948; Ellison and Turner, 1960; Pacanowski and Philander, 1981) but good data to test these forms have been lacking in the ocean.

The nondivergent, steady state turbulent energy equation may be expressed as

$$K/K_M = Rf/Ri \tag{9}$$

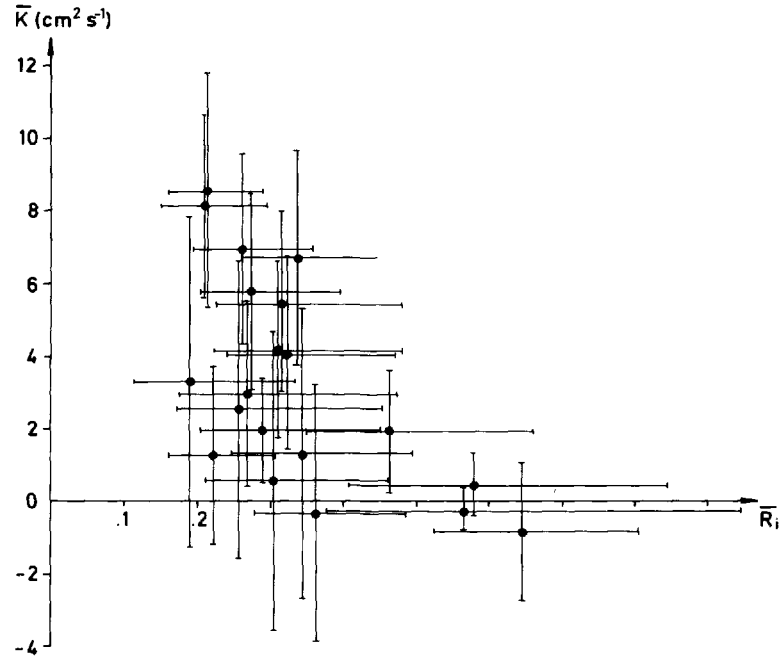

Figure 10. The mean coefficients of turbulent heat diffusion, $\overline{K}$, plotted against corresponding values of the mean Richardson numbers, $\overline{Ri}$. Error bars are given by ±.5 standard deviation for $\overline{K}$ and by $\overline{Ri}_{\min}$, $\overline{Ri}_{\max}$ (defined in text) for $\overline{Ri}$.

where K_M is the turbulent exchange coefficient for momentum, and the others are defined as above (K for density and temperature taken to be equivalent here). We want (Turner, 1973),

$$K/K_M \rightarrow 1$$

and

$$K/K_M \rightarrow Rf_{\text{crit}}/Ri \quad \text{as } Ri \rightarrow \infty$$

where Rf_{crit} is a small constant value as supported by experiments, see Osborn (1980) for discussion. Perhaps the simplest form satisfying these conditions is

$$K/K_M = 1/(1 + \nu\, Ri) \tag{10}$$

whereby

$$Rf = Ri/(1 + \nu\, Ri)$$

and

$$\nu = Rf_{\text{crit}}^{-1}$$

Table 1. Parameter choices giving the least mean squares, best fit to the stationwise ($n = 20$) mean coefficient of turbulent heat diffusion and Richardson number data to the relation $K = K_0/(1 + \nu Ri)^p$. σ_K is the standard deviation of the data from the best fit curves. The underlined parameters were chosen before each calculation.

	$K_0(\text{cm}^2\,\text{s}^{-1})$	$\nu(=Rf_{\text{crit}})^{-1}$	p	$\sigma_K(\text{cm}^2\,\text{s}^{-1})$
$n = 20$,	32	5	2.4	2.25
no	49	10	1.9	2.26
weighting	50	5	2.9	2.28
$n = 20$,	38	5	2.5	2.33
Inverse area	60	10	2.0	2.34
weighting	50	5	2.8	2.34

The particular choice of (10) has no deeper justification than consistency with the limit conditions above and its simplicity but yields, for instance, functional curves essentially identical with those of Ellison and Turner, (1960), based on Ellison's (1957) model for $Ri > .1$ (except that they find $K/K_M = 1.4$ at $Ri = 0$).

The following choices are consistent with (10):

$$K = K_0/(1 + \nu\, Ri)^p \tag{11}$$

$$K_M = K_0/(1 + \nu\, Ri)^{p-1} \tag{12}$$

where K_0 is the neutral stability turbulent exchange coefficient which is $\tau\rho^{-1}S^{-1}$ where τ is a (boundary layer) stress (Turner, 1973).

The advantage of the above approach is that it identifies ν as inverse of the critical flux Richardson number and thus provides a basis for choosing it. In some chosen $K(Ri)$, for instance the much quoted Munk and Anderson (1948) one, the "ν's" are chosen to be different for K and K_M. Their choice leads to an Rf_{crit} of .53 which appears to be too large in the light of recent experimental evidence. In addition recent investigations (eg. Pacanowski and Philander, 1981) and the present one indicate that the M and A choice of $p = 1.5$ is probably too small.

The parameter choices giving the least squares best fit of the functional relationship of $K(Ri)$ given by (11) to unweighted and weighted data are listed in Table 1. The data base is the original $\overline{K}$ data of Figure 6a and corresponding $\overline{Ri}$ corrected for bias ($\overline{Ri}^*$ of Table A2). In the first two runs of each case ν was chosen as 5 and 10 (corresponding to $Rf_{\text{crit}} = .2$ and .1) and K_0 and p were determined by least squares best fit. In the third run K_0 and ν were chosen as 50 $\text{cm}^2\,\text{s}^{-1}$ and 5 respectively and p was determined by the best fit. σ_K is the standard deviation of the data from the least mean squares curve. In the first case the 20 data points were considered unweighted. In the second case each point was weighted by the inverse of the area of the rectangle formed by the outer bounds of the error bars of $\overline{K}$ and $\overline{Ri}$ where these are as given by $\overline{K} \pm \sigma_K$ and by $\overline{R}_{\text{min,max}}$ corrected for bias ($\overline{Ri}^*_{\text{min,max}}$ in Table A2). The data points and some of the least mean square curves are shown in Figure 11 (the curves nicely avoid hitting the data points).

Table 2. Horizontally-averaged (Boxes 1-4 and 4-7), mean coefficients of turbulent heat diffusion, its standard deviations, Richardson numbers and minimum and maximum Richardson numbers (as defined in the text) for the chosen temperature ranges.

	T(°C)	$\overline{K}$(cm^2 s^{-2})	σ_K(cm^2 s^{-1})	$\overline{Ri}$	$\overline{Ri}_{min}$	$\overline{Ri}_{max}$
Box	>15.8	5.70	6.06	.211	.149	.297
1-4	15.2–15.8	4.00	5.26	.319	.224	.496
	14.7–15.2	2.12	4.25	.256	.190	.358
	14.4–14.7	—	—	.219	.145	.374
	<14.4	—	—	—	—	—
Box	>15.8	4.14	6.44	.306	.231	.414
4-7	15.2–15.8	3.18	5.90	.343	.257	.473
	14.7–15.2	1.83	5.39	.390	.314	.499
	14.4–14.7	.56	3.11	.576	.447	.767
	<14.4	.09	1.15	.840	.590	1.212

It was shown in Appendix 2 that further horizontal averaging should help increase the accuracy (although decrease the horizontal resolution) of the results. For this reason the $\overline{K}$ results for boxes 7-5, 6-4 and 4-2, 3-1 were averaged and $\overline{Ri}$ was recalculated for the stations 1–4 and 4–7. These new $\overline{Ri}$ were corrected for bias and presented in Table 2. Comparison with earlier results show a general improvement in the signal to noise ratio. The 90% confidence interval on $\overline{Ri}$ (not shown) also narrowed by roughly 50%. These new $\overline{K}$ and $\overline{Ri}$ form the data base for a new, least mean squares best fit calculation, the results of which are given in Table 3. Included is the no weighting, tidal "correction" case, which uses the $\overline{K}$ calculated from the tidal

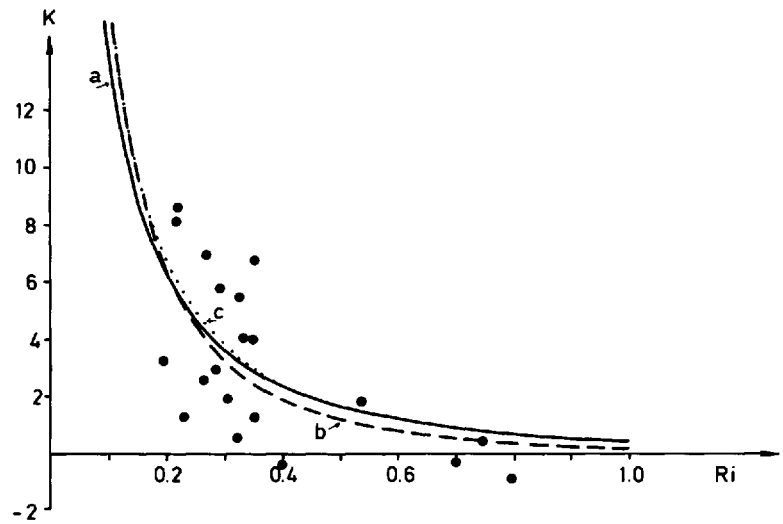

Figure 11. Best fit $K(Ri)$ curves for the model $K = K_0/(1 + \nu Ri)^p$ for the cases $\nu = 10$ (a), $K_0 = 50$ cm^2 s^{-1} and $\nu = 5$ (b), inverse area weighting, $\nu = 10$ (c) for the stationwise data.

Table 3. As Table 1 but with horizonally-averaged (Box 1-4 and 4-7, $n = 8$) mean coefficient of turbulent heat diffusion and Richardson number data. New are the no weighting, tidal "correction" case results (see text).

	$K_0(\text{cm}^2\,\text{s}^{-1})$	$\nu(=Rf_{\text{crit}})^{-1}$	p	$\sigma_K(\text{cm}^2\,\text{s}^{-1})$
$n = 8$	32	$\frac{5}{}$	2.5	.93
no	52	$\frac{10}{}$	2.0	.94
weighting	$\frac{50}{}$	$\frac{5}{}$	3.0	.94
$n = 8$	$\overline{39}$	$\frac{5}{}$	2.8	.81
Inverse area	63	$\frac{10}{}$	2.2	.82
weighting	$\frac{50}{}$	$\frac{5}{}$	3.1	.82
$n = 8$	$\overline{23}$	$\frac{5}{}$	2.0	.99
no weighting	33	$\frac{10}{}$	1.6	.99
tidal	$\frac{50}{}$	$\frac{5}{}$	2.9	1.09
"correction"				

"corrected" original data ($\Theta_1 = 341°$ and $\Theta_{2,3} = 327°$ see Appendix 2). Note that the standard deviations are much reduced in this horizontally averaged calculation. This is shown more graphically in Figure 12 where most of the points are hits or near hits for the curves. Also shown are the points resulting from the tidal "corrected" data.

The weighted and unweighted cases, for $n = 20$ and for $n = 8$, are quite similar yielding K_0 in the range of 32–39 $\text{cm}^2\,\text{s}^{-1}$ and p in the range 2.4–2.8 for $Rf_{\text{crit}} = \nu^{-1} = .2$ and K_0 in the range of 49–63 $\text{cm}^2\,\text{s}^{-1}$ and p in the range of 1.9–2.2 for $Rf_{\text{crit}} = \nu^{-1} = .1$. A good fit was also found for $K_0 = 50\ \text{cm}^2\,\text{s}^{-1}$ and $Rf_{\text{crit}} = \nu^{-1} = .2$ with $p = 2.9$–3.1 for these cases. The tidal correction, $n = 8$ results were somewhat lower than the others but would be raised somewhat, by an inverse area weighting. Based on these results, the

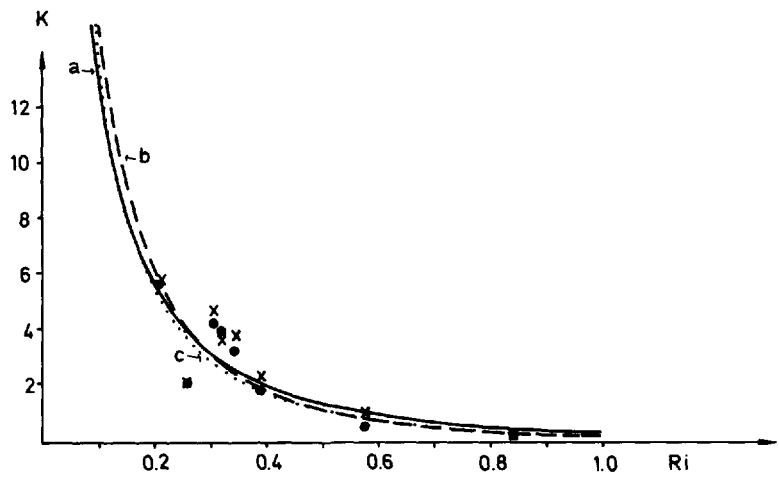

Figure 12. Best fit $K(Ri)$ curves for the model $K = K_0/(1 + \nu Ri)^p$ for the cases $\nu = 10$ (a), $K_0 = 50\ \text{cm}^2\,\text{s}^{-1}$ and $\nu = 5$ (b), inverse area weighting, $\nu = 10$ (c) for the box 4-1, box 7-4 data. In addition data for points for the tidal correction case are shown as crosses.

following set of parameters is my "best choice"—$K_0 = 50\ \mathrm{cm^2\,s^{-1}}$, $R f_{\mathrm{crit}} = \nu^{-1} = .1$ and $p = 2$. Note that any parameter set in Tables 1 and 3 yields very similar $K(Ri)$.

5. Estimations of coastal upwelling circulation from the Richardson number

Figures 2, 3 and 6 and the error discussion in Appendix 2 reveal considerable uncertainty in the $t - x - T$ structure of $\overline{w}_D$ and $\overline{K}$ from the NCCM calculation. The modest time resolution of the experiment made it difficult to resolve the net inflow M into the boxes. Still, the general $x - T$ structure of the diapycnal exchanges was consistent, made sense and seemed to serve well to "calibrate" a $K(Ri)$ relationship. The $t - x - T$ structure of Ri statistics and $\overline{Ri}$ as shown in Figures 3, 8 and 9 appeared to be better behaved. This $\overline{Ri}$ information is used below in an inverse approach to arrive at new $x - T$ distributions of $\overline{w}_D$ and $\overline{K}$, expected to be "better" than the original ones.

Figure 13 shows $\overline{K}[\overline{Ri}]$ from the "best choice" $\overline{K}(\overline{Ri})$ and $\overline{Ri}$ from Figure 8. The comparison of these results with NCCM $\overline{K}$ in Figure 6a shows general agreement but somewhat lower $\overline{K}$ at the base of the frontal layer with considerably lower values in the T range 15.2–15.8 directly below. Nearshore $\overline{K}$ were higher with a subsurface $\overline{K}$ maximum in the lower layers nearshore. By differentiating (6) and averaging in time we have

$$\overline{w}_D = \overline{-C^{-1}\partial(C\,K\,\partial T/\partial z)/\partial T} \approx \partial(\overline{K}\,\overline{\partial T/\partial z})/\partial T \tag{13}$$

since C is constant and $\partial T/\partial z$ is quite invariant with time away from the mixed layers and the vicinity of the coast. Figure 14 shows $\overline{w}_D[\overline{K}(\overline{Ri}), \overline{\partial T/\partial z}]$ calculated from (13) with $\overline{K}(\overline{Ri})$ from Figure 13 and $\overline{\partial T/\partial z}$ formed by averaging as for $\overline{Ri}$ earlier. Note that $\partial/\partial T$ has been estimated by $\Delta/\Delta T$, and thus $\overline{w}_D$ falls approximately on the T boundaries of the bins, ~15.8, 15.2, 14.7 and 14.4°C, as indicated in Figure 14. The comparison of these $\overline{w}_D$ with NCCM $\overline{w}_D$ (Fig. 2a) shows how sensitive the upwelling is to the magnitude and vertical structure of $\overline{K}$. $\overline{w}_D(\overline{K}(\overline{Ri}), \overline{\partial T/\partial z})$ is reduced by a factor of 2 at the base of the frontal layer and by a factor of 4 or more below. The values offshore are more similar.

From $\overline{w}_D\,(x, T)$ and the assumption that, integrated over the alongshore scale of the line separation, 62 km, upwelling is fed by cross-shelf flow (as indicated in P1), the mean upwelling circulation in the $x - T$ plane can be determined. The procedure is to integrate $\overline{w}_D$ from the coast seaward along every isothermal surface to obtain the total diapycnal transport as a function of x and T. Contours of constant transport are then upwelling circulation streamlines. One problem here is that the observed variability of C and $\partial T/\partial z$ in the zone just adjacent to the coast makes a calculation of $\overline{w}_D$ there from (13) dubious even if the $\overline{K}$'s were known well. For the subsequent calculation I extrapolate the $\overline{w}_D$, at station 2 to the coast and argue that the error made in doing this is not likely to be great since this zone is so only ~3–5 km wide and since the values at station 2 should approximate $\overline{w}_D$ near the coast. More convincing is the argument in P1

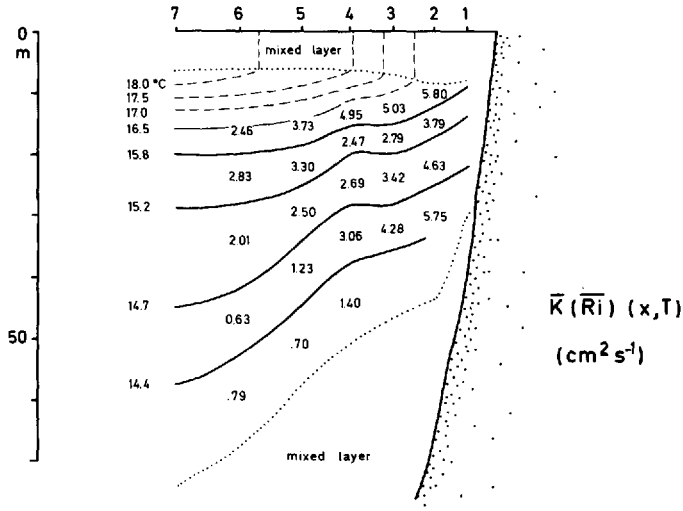

Figure 13. Mean coefficients of turbulent heat diffusion, $\overline{K}$, based on the best fit $K(Ri)$ model listed at their x-T positions.

as supported by the results here that much of the "coastal" Ekman divergence is, in fact, displaced seaward in the study area.

Figure 15a shows the mean coastal upwelling circulation pattern obtained from the NCCM $\overline{w}_D$. The transport streamlines have a separation of .2 $m^2\ s^{-1}$. This can be compared with $\overline{u}\ (x, T)$ in Figure 16 formed by averaging the original current data

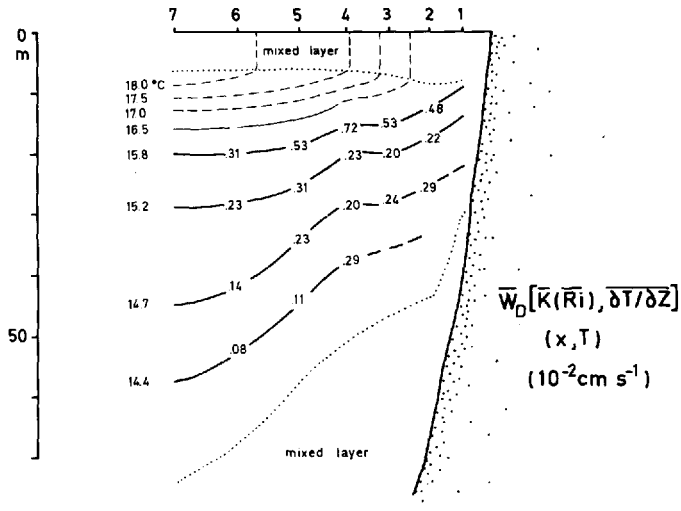

Figure 14. Mean diapycnal vertical velocities, $\overline{w}_D$, based on the best fit $K(Ri)$ model and $\overline{\partial T/\partial z}$ and listed at their x-T positions.

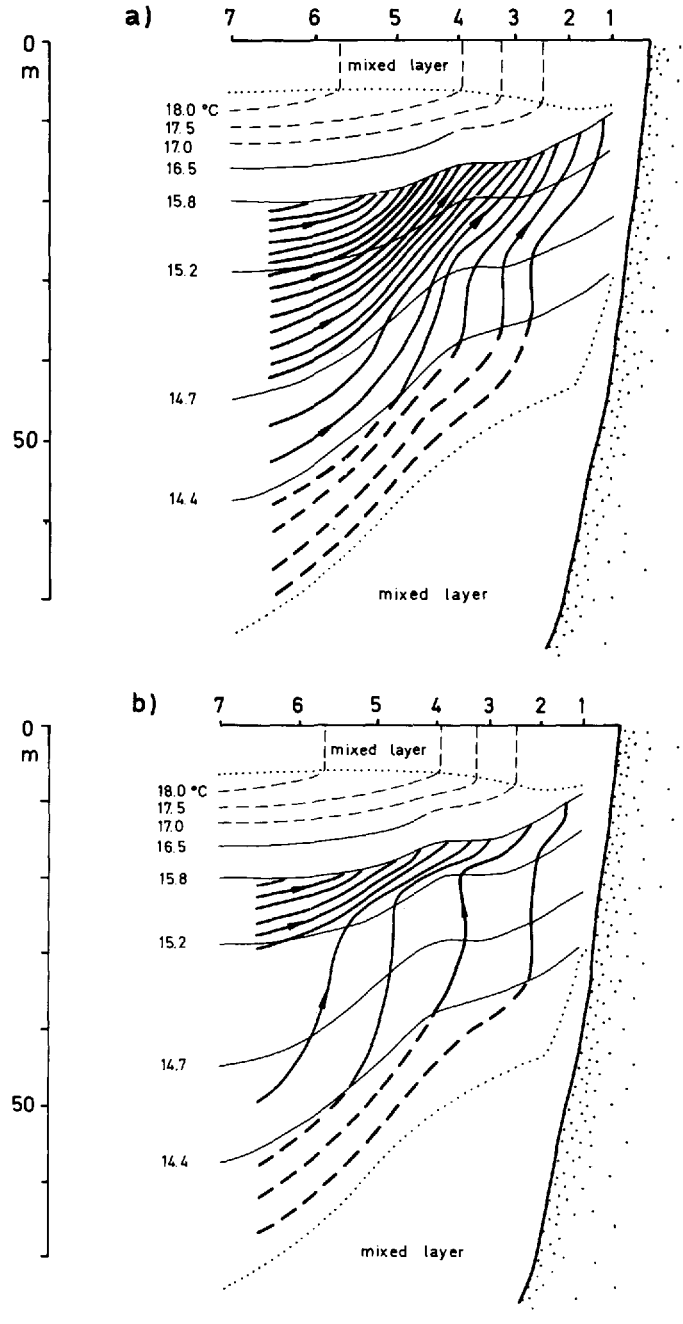

Figure 15. Mean transport streamlines for the coastal upwelling circulation based on the NCCM results (a), the best fit $K(Ri)$ model results (b) and K = constant = 7 $cm^2\ s^{-1}$. (c). Distance between the streamlines is .2 $m^2\ s^{-1}$.

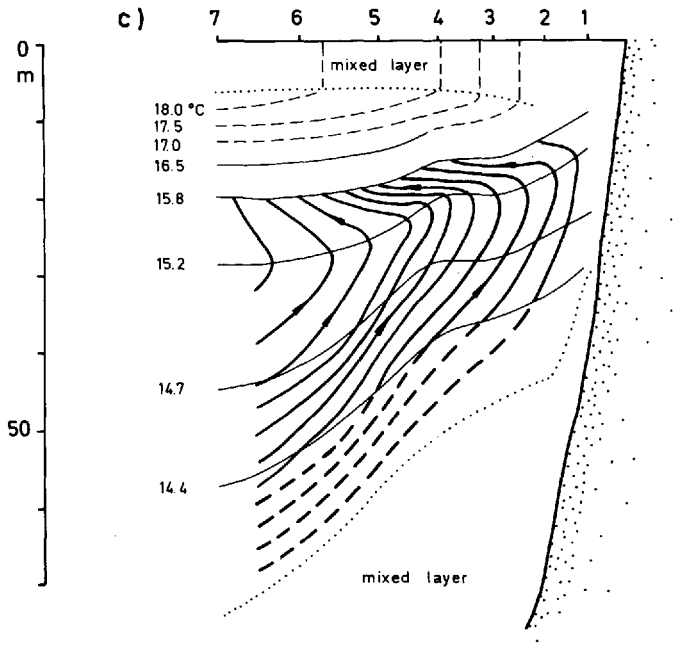

Figure 15. (Continued)

from the five sections in each of the two lines in x, T space and plotting the results on our basic mean thermal field. The vertical structure of mean shoreward flow in both Figures 15a and 16 agree well and minima and maxima of shoreward flow coincide. However the shoreward speeds calculated for the upper layers in the offshore and central regions, ~10–15 cm s^{-1}, were about double those for $\bar{u}$. This effect is associated with the upwelling center near the base of the frontal layer with NCCM $\bar{w}_D$, 1–1.5 × 10^{-2} cm^2 s^{-1}. Vertical velocities associated with the observed alongshore divergence of the alongshore flow (i.e. from Fig. 4a and b in P1) are small, ≤.2–.3 × 10^{-2} cm^2 s^{-1}. Thus, this disagreement is probably due to uncertainties in the NCCM calculation. The total transport through the 15.8°C isothermal surface in Figure 15a is 4.2 m^2 s^{-1}, about twice the mean Ekman transport of 2.3 m^2 s^{-1} calculated from local wind observations (P1). The total shoreward transport calculated from $\bar{u}$ above the bottom mixed layer in Figure 17 for stations 7-5, however, is 2.0–2.5 m^2 s^{-1} in good agreement with the calculated mean Ekman transport.

Figure 15b shows the coastal upwelling circulation which results from the "best choice" $K(Ri)$ model, ($\bar{w}_D$ in Fig. 14). It shows quite strong, shoreward flow, 10–15 cm s^{-1} in the temperature interval 15.2–15.8, upwelling centered at the base of the frontal layer, weak inflow in the T range 14.4–15.7 and implies moderate inflow, ~5 cm s^{-1} below 14.4°C. Except for the weak inflow in the T range 14.7–15.2 in the offshore region, the circulation structure agrees with that calculated in Figure 15a and implied

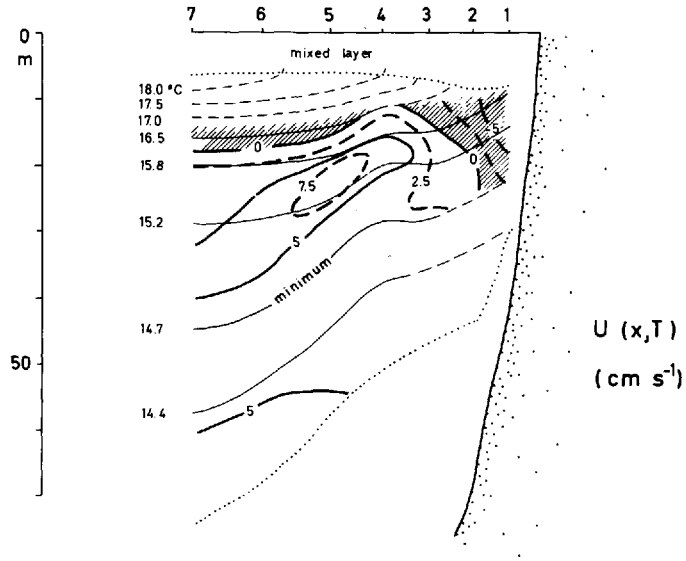

Figure 16. Mean shoreward flow over the study period plotted on the mean thermal field.

in Figure 16. In this case, however, total transport through the 15.8°C isothermal surface is 2.1 $m^2 s^{-1}$ in good agreement with the calculated mean Ekman transport.

Further calculations were made with different choices of $\overline{K}$ to test the sensitivity of the mean coastal upwelling circulation to the $\overline{K}$ distribution with the same observed $\overline{\partial T/\partial z}$. Figure 15c shows the results for $K = 7$ $cm^2 s^{-1}$, the constant value at which the total transport through the 15.8° isothermal surface equaled the calculated mean Ekman transport. The circulation is radically changed with the near-surface upwelling shifted seaward, the inflow concentrated below $T = 14.7°$ and a strong, *seaward* flow, ~10–15 cm s^{-1}, at the base of the frontal zone. In this case, upwelling is inversely proportional to the vertical separation of isothermal surfaces. Clearly this circulation does not agree with the observations.

Another choice of K, K_M dependency originating from Fjeldstad (1964) is K, $K_M = a N^{-2}$, where a is constant (e.g., Martinsen and Weber, 1981; McCreary, 1981). This choice, used for mathematical convenience, has some peculiar physical ramifications: it implies ϵ = constant from the turbulent energy equation and f = constant from (5). In a stratified ocean of constant depth this means $w_D = GC^{-1} = -(c_p C)^{-1} \partial F/\partial T = 0$ and there is no upwelling circulation. The Munk and Anderson (1948) $K(Ri)$ model was tried and found to model the structure reasonable well but satisfied the Ekman transport for $K_0 = 13$ $cm^2 s^{-1}$, an unlikely low value.

6. Heat balance

The equation of heat conservation in temperature space is one of the bases of the NCCM calculations. Together with mass conservation it enabled the calculation of $\bar{f}$

and $\overline{w}_D$ below $T \sim 15.8°C$ earlier. Here we will consider the heat balance of the surface layers above $T \sim 15.8°C$. The results here (Fig. 2a and 4a) and in P1 (Fig. 3a–d) showed that the 15.8° isotherm surface was quite stationary in time over the study period and we can express the mean heat balance per unit area in the surface layer to good approximation as

$$c_p \hat{\bar{D}}(\hat{T}_2 - \hat{T}_1)/\tau = c_p\Big[C^{-1}\int_\eta \int_D^0 \overline{u}_n\, \overline{T}(\eta, z)\, dz'd\eta' + \overline{w}_D \cdot 15.8° \text{ C}\Big] + \bar{f} + \bar{q} + \Gamma \tag{14}$$

where $\hat{\bar{D}}$ is the time and space averaged depth to 15.8°C, $\hat{T}_1$, $\hat{T}_2$ are the volume-averaged temperatures at the beginning and end of the time period τ respectively, $\overline{u}_n$ is the horizontal velocity normal to the vertical sides of the volume being considered, η is a coordinate along these sides, $\bar{q}$ is the mean surface heat flux per unit area, Γ is the horizontal turbulent heat transport per unit area across the vertical sides of the volume where

$$\Gamma = c_p\, C^{-1} \int_\eta \int_D^0 \overline{u_n' T'}\, (\eta, z)\, dz'd\eta'. \tag{15}$$

Here, u_n' and T' are fluctuations about time mean $\overline{u}_n$ and $\overline{T}$ and all other variables are as defined earlier.

Alongshore divergence was found to be small and therefore

$$\int_\eta \int_D^0 \overline{u}_n\, \overline{T}(\eta, z)\, dz'd\eta' \approx (\xi_k\, \overline{U}_k\, \hat{\bar{T}}_k - \xi_j \overline{U}_j\, \hat{\bar{T}}_j)/(\Delta x_{j,k}) \tag{16}$$

where $\overline{U}_j = \int_{D_j}^0 \overline{u}_j\, dz'$ and $\hat{\bar{T}}_j = \int_{D_j}^0 \overline{T}_j\, dz$ at x_j, ξ_j is a form factor defined by $\xi_j = \int_{D_j}^0 \overline{u}_j\, \overline{T}_j\, dz / \overline{U}_j\, \hat{\bar{T}}_j$ and $\Delta x_{j,k}$ is the distance between stations j and k ($j > k$).

A reasonable range of variation for ξ_j would be from 1 for uniform seaward Ekman flow above 15.8° to $\overline{T}_{\text{mix}j}/\hat{\bar{T}}_j$ where $\overline{T}_{\text{mix}j}$ is the mean temperature in the surface mixed layer at station j. The latter case corresponds to seaward Ekman flow in the surface mixed layer only. In the following, the average of these two extremes is used. Both $\overline{T}_{\text{mix}j}$ and $\hat{\bar{T}}_j$ are calculated from our temperature profiling results in the upper layer by first averaging between lines A and B at station j and subsequently averaging in time. Note that $\overline{U}_j$ can be identified as $\int_0^{x_j} \overline{w}_D\, (T = 15.8°C)\, dx$, the total mean upwelling through the 15.8°C isothermal surface shoreward of x_j and thus can be calculated directly from the $\overline{w}_D$ distributions determined earlier. Wyrtki (1966) calculated $\bar{q}$ to be 150–175 Wm^{-2} in the study area in December. His analysis was based on two degree squares and it is likely that $\bar{q}$ for the zone of coldest water just adjacent to the coast is, in fact, greater than this. Here we take $\bar{q} = 250\ \text{Wm}^{-2}$ as a reasonable upper bound.

Table 4 shows the results of several heat balance calculations based on (14), (16) and the discussion above. In particular the surface layers of boxes 1–4 and 4–7 are

Table 4. Results of the surface layer heat conservation calculations based on NCCM and $K(Ri)$ model circulation results. The first term is the rate of change of heat storage, the second is the heat advection, f is the diapycnal turbulent heat flux, q is the surface heating and Γ, the sum of the other terms, is the shoreward horizontal eddy heat flux. Units are Watt m^{-2}.

	Box	$c_p\hat{\bar{D}}(\hat{T}_2 - \hat{T}_1)\tau^{-1}$	$c_p[(\xi_K\bar{U}_K\hat{\bar{T}}_K - \xi_j\bar{U}_j\hat{\bar{T}}_j)(\Delta x_{j,K})^{-1} + \bar{w}_D 15.8^0]$	$\bar{f}$	$\bar{q}$	Γ
NCCM	1-4	17	−546	−395	≤250	≥708
	4-7	23	−941	−361	≤250	≥1075
$K(Ri)$	1-4	17	−294	−284	≤250	≤340
	4-7	23	−537	−247	≤250	≥557

considered for the NCCM and the "best choice" $K(Ri)$ determinations of $\bar{w}_D$ and $\bar{f}$. The eddy heat flux per unit area, Γ, is the sum of the other, "known" terms. Since alongshore temperature gradients were small, Γ in Table 4, indicates shoreward eddy heat flux and exceeds surface heating rate per unit area by a factor 1.5–4. With the usual parameterization $\overline{u'T'} = K_H \cdot \overline{\partial T/\partial x}$, the Γ's from Table 5 and observed surface layer $\overline{\partial T/\partial x}$, values of 1.5–3.0 × 10^7 cm^2 s^{-1} and 4–6 × 10^7 cm^2 s^{-1} emerge for K_H, the coefficient of horizontal turbulent heat diffusion, at stations 4 and 7 respectively. Furthermore it was observed that when the winds slackened during the middle of the study period, warm surface layer water with temperatures exceeding the former ones by ~1°C impinged upon the coast. Taking T' = 1°C and from Γ's in Table 5 we get $c_r u' \approx$ 10–20 cm s^{-1} and 24–36 cm s^{-1} for stations 4 and 7 respectively. If we take c_r, the correlation coefficient to be, say, .8 for this event we get $u' \sim$ 12–25 cm s^{-1} and 30–45 cm s^{-1} for stations 4 and 7. The lower part of this range of values for station 4 is in good agreement with near-surface standard deviations observed during our data set, (Fig. 5c and d in P1). On the other hand u' at station 7, particularly that from the NCCM calculation, appears too large. Again this favors the $K(Ri)$-based results.

7. Discussion

The purpose of this paper was to study the diabatic, nonreversible aspects of coastal upwelling over the wide shelf off Peru. Here the natural coordinate conservation method (NCCM) was applied in an attempt to quantify diapycnal advection and diffusion. The results presented in parts 3 and 4 showed that (1) vertical velocities across isopycnals were much greater than vertical velocities associated with the flow along sloping isopycnals and (2) upwelling and internal mixing appeared to be greatest at the base of the frontal layer. The error analysis given in Appendix 2 showed that neither random errors due to instrument uncertainties nor tidal aliasing were large sources of error. Accuracy was limited by difficulties in resolving inflow into the boxes but was improved by averaging.

The distribution of means and statistics of the Richardson number, Ri, was also considered as an alternative, independent approach for studying internal mixing. $\overline{Ri}$,

defined by $\overline{N}^2/\overline{S}^2$ where $\overline{N}^2$ is the mean buoyancy frequency squared and $\overline{S}^2$ is the mean squared velocity shear, was found to have a distribution like that of NCCM $\overline{K}$ and of the statistic $\%Ri < .25$ (x, T). The latter result indicated that, in general, $\overline{Ri}$ formed above was representative for the mean turbulent conditions. Also this and the magnitude of NCCM K implied that the upwelling coastal corner was characterized by rather high levels of turbulence creation analogous for example to what is thought about equatorial regions (eg., Crawford, 1982). The creation rate appeared to have a well-defined, stable x, T structure. Another striking result was the strong, "immediate" response of the rate of turbulence generation, as inferred by the time development of the $\%Ri < .25$ statistic, to changes in the local alongshore wind stress. The minimum $\%Ri \leq .25$ frequency occurred during the middle of the study period when currents were actually strongest. These, however, were associated with a *barotropic,* poleward flow event (P1). The deepening of the bottom mixed layer associated with this event (P1) implied a maximum in bottom boundary layer turbulence generation then and an interesting phase shift with respect to the intensity of the shear generation of turbulence within the thermocline.

Our results indicate that Ri was more controlled by S^2 than by N^2 in the coastal corner, fully-developed coastal upwelling system here. One would indeed expect that changes in turbulent intensity should be intimately coupled to the wind changes through changes in current shear. This can be readily understood in terms of the fast response of the Ekman layer and the shear at the base of it to changes in alongshore wind stress. In fact Richardson numbers formed from the mean stratification and the square of the mean shear at the base of the Ekman layer were typically below 1 in the study area (see Fig. 7 in Shaffer, 1982). A Richardson number formed from the square of the mean shoreward shear at the base of the shoreward "jet" in the same figure is even lower, ~.5, pointing out that this jet is probably frictionally-controlled and also may respond rapidly to wind changes. Note that in the study area as opposed to other regions of coastal upwelling, for instance off Oregon (Johnson *et al.,* 1976), the shear of the shoreward flow appears to be at least as important for shear turbulence generation as that of the alongshore flow. A corollary to this is that, again as opposed to common wisdom regarding coastal upwelling regions, internal friction, and not just geostrophy in this region of quite small Coriolis parameter, may play an important dynamical role for at least the baroclinic part of the alongshore flow.

Different choices for $K(Ri)$ were discussed and a relation suggested which, although similar in form to those proposed previously, underlines the role of the flux Richardson number. The chosen functional form was then "calibrated" in a least mean square, best fit sense with the NCCM $\overline{K}$ and the $\overline{Ri}$. "Best fit" parameters actually lead to a $K(Ri)$ relationship which is identical (except for a small, "background" mixing constant) to the one chosen by Pacanowski and Philander (1981) on the bases of best fit to observations of a numerical model of the response of equatorial oceans to different wind stress patterns. Although this could be fortuitous, both results do stem from

regions characterized by rather high, rather steady turbulence creation. This agreement and the robustness of our $K(Ri)$ results to different reasonable weighting and averaging schemes embolden me to suggest that the $K(Ri)$ form in (13) with the set of best fit parameters obtained here may define a universal $K(Ri)$ relationship: Other $\overline{Ri}$ calculated as above ($\overline{Ri} = \overline{N}^2/\overline{S}^2$, vertical separation scale ~5–10 times the Ozmidov length, sufficient averaging to characterize the turbulent state) should yield reliable values for $\overline{K}$ anywhere else in the ocean with high levels of turbulence creation; i.e., $\overline{Ri}$ in the range ~.1–1.

From $\overline{K}$, $\overline{\partial T/\partial z}$ and the isothermal surface area, $\overline{w}_D$ can be calculated. Such $\overline{w}_D$, the assumption of cross-shelf mass balance over the alongshore scale considered and the boundary condition of no flow through the bottom determine total diapycnal transport as a function of x and T. Isolines of this transport are upwelling circulation streamlines. This circulation was calculated from our $K(Ri)$ model and compared with a circulation calculated from NCCM results, with the original $\overline{u}(x, T)$, and with circulations resulting from other choices of K. Agreement in structure between the NCCM and $K(Ri)$-based circulation was good but the latter agreed best with Ekman transports calculated from shore-based wind observations. The coastal upwelling circulation was found to be quite sensitive to the choice of K. A circulation based on constant K bore little resemblance with $\overline{u}(x, T)$.

The heat balance in the surface layers of the study area was also studied. Substantial shoreward eddy heat flux, supplying more heat per unit area than surface heating, was needed for heat conservation. Implications of the heat balance calculation for current and temperature fluctuations in the surface layer and coefficients of horizontal turbulent heat exchange again favored the $K(Ri)$-based circulation.

The total picture of the upwelling coastal corner is one of a self-regulating system quite sensitive to changes in the forcing functions. Strong surface layer heating from surface heating and shoreward eddy heat fluxes tend to increase the stratification while strong internal mixing works to weaken it. The observed stratification is the result of the struggle between these two tendencies. A decrease in wind leads to decreased shears, weakened mixing and subsequent rapid warming of the surface layers. A wind increase leads to increased shears, increased mixing and rapid surface cooling. The sensitivity of K to the current shears through the $K(Ri)$ relationship implies that for every set of surface layer heating-wind forcing conditions there exists a certain stratification, internal mixing structure and coastal upwelling circulation. This, of course, is constrained by the basic stratification and flow of the eastern ocean boundary circulation. It was argued in Shaffer (1982) that Ekman pumping out of the bottom mixed layer due to the observed barotropic poleward jet adjacent to the coast helped compress the shoreward compensation flow vertically. This would lead to increased turbulence generation through increased vertical shear.

One striking feature exhibited in the upwelling circulations, based on both the

NCCM and the $K(Ri)$ model, was the seaward displacement of the upwelling into the surface layer. Models often take the Ekman divergence to be at the coast, even as a point sink (eg., Allen, 1973; Pedlosky, 1978). Although winds blowing over the ocean were not observed during our study and our circulation results were most uncertain just adjacent to the coast, this seaward displacement is consistent with the arguments in Shaffer (1982) in terms of larger "effective" Coriolis parameter, due to the horizontal shear of the poleward jet, and a reduced drag coefficient associated with the coldest water and greatest stability in the air adjacent to the coast. This implies a rather quiescent, but highly productive narrow zone at the coast which may present optimal conditions for first-feeding larvae of the enormous pelagic fish stocks found over the wide shelf off Peru.

The mean coastal upwelling circulation has been an elusive creature subject to much speculation but little identification. Discussion has raged back and forth between two-cell and non-two-cell supporters (eg., Mooers *et al.*, 1976 and Smith, 1981) where thumbs down or up have often been hung on a precarious thread of a several degree coordinate axis rotation. Several recent numerical models (Foo, 1981; Endoh *et al.*, 1981, and Kundu, 1984) with Munk and Anderson's K parameterizations or second-order turbulence model components have demonstrated vertical structure in the shoreward flow due to "internal" Ekman layers. Structures like this were also observed in our study area (again Fig. 7 in Shaffer, 1982) but no mean seaward currents within the thermocline. As the results of these models and our diagnostic, upwelling circulation results here show, such structure is not associated with a closed double cell circulation but rather represents a meandering of the water being upwelled as it finds its way to the surface. Long-term experiments with recording current meters in other regions of coastal upwelling such as northwestern Africa, Oregon and near 15°S off Peru show little vertical structure in the shoreward flow (Smith, 1981). However for such measurements at fixed points in space, weak mean vertical structure coupled with certain thermocline layers would tend to be smoothed out by large, essentially adiabatic fluctuations of current and stratification; i.e., due to the passage of coastal-trapped waves, moving up and down by the fixed points. Indeed it may often be difficult with such methods to capture the mean shoreward flow. Emboldened by the apparent success of the $K(Ri)$ model for calculating the diagnostic coastal upwelling circulation, success which could be documented in this region of quite steady flow, I propose that it may be more meaningful to deploy an Ri profiler (or other profilers capable of yielding good K results) in an upwelling region than to moor many recording current meters at fixed points there if the mean upwelling circulation is to be studied.

Acknowledgments. The author wishes to thank all those at the Institute of Oceanography, University of Gothenburg who helped with the preparation of this manuscript. Flowers are presented especially to Ola Akerlund for ambition and patience. Financial support of the Swedish Natural Science Research Council is gratefully acknowledged.

APPENDIX 1

Application of the natural coordinate conservation method to the wide Peruvian shelf data set

The natural coordinate conservation method was applied to the following set of boxes formed from sequences of stations in each of lines A and B: 3-1, 4-2, 5-3, 6-4, and 7-5, Box 6-4 is shown in Figure 1. Such overlapping boxes were a trade off between good resolution in the x direction and sufficient accuracy in the outputs of the method. With the above set of boxes the cross-shelf current information from every station is used and the boxes are hopefully wide enough to smooth out some of the smaller horizontal scale "noise." The effects of forming larger boxes from the data set is investigated in part 5.

Fixed positions were chosen for each station and data from each section were interpolated linearly to each of these positions from the two profiling observations straddling it. Stations A1, B1 and A7, B7 were taken at the outermost and innermost position occupied during the study to avoid extrapolation at the end points. With these choices the surface areas of each box as well as the direction of the normals to each of its straight sides are fixed.

Since lines A and B were occupied in general on alternating days a choice of interpolation in time had to be made for calculating daily values. Figure A1 illustrates the choice made for the subsequent calculations. Earlier calculations made with the pairs A, 1-B, 1, etc. yielded similar mean results but the choice used here should tend to smooth out some of higher frequency (several day) "noise."

Thus (1) can be written

$$G_{i,j} = M_{i,j} - (V_{i+1,j} - V_{i-1,j})(t_{i+1} - t_{i-1})^{-1} \tag{A1}$$

where $i = 1, 8$ identifies the day t_i and $j = 1, 5$ identifies the box such that $j = 1$ is box 3-1, etc. For the end points in time, t_1 and t_8, V_{i-1} resp V_{i+1} are calculated from A, 1-B, 1 resp A, 5-B, 5 alone and $t_{i+1} - t_{i-1} = 1.5$ days.

$M_{i,j}$ is calculated for each t_i as follows:

1. For every current and temperature profile observation the components u and v are calculated, interpolated linearly in the vertical and read off together with T at fixed depths in steps of 1 m from the bottom to the depth of the uppermost current meter. The current is set to zero at the bottom. v is directed normal to the lines; i.e., $+v \rightarrow 327°$. u is directed at an angle normal to the nearest alongshore box side; i.e., a side like the one formed by A6–B6; $+u$ ranges from 52.5° at A1–B1 to 49° at A7–B7.

2. Partial transports normal to the lines and the alongshore box sides are then calculated for all T in .1°C steps from $T_0 = 13.7$°C to T_{max}, the temperature at the

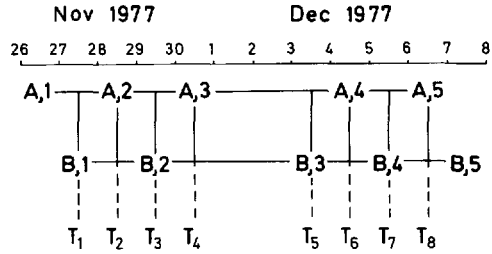

Figure A1. Sketch of time interpolation scheme for the NCCM calculations.

depth of the shallowest current meter, from the expressions

$$M^{r,1}, M^a(x, T) = \sum_{z_B}^{z(T)} (v(z)\ L^{r,1}, u(z)\ 31\ \text{km})\ \Delta z \qquad \text{(A2)}$$

Where $L^{r,1}$ is half the distance to the profile observation immediately shoreward resp. seaward of the observation in question, z_B is the bottom depth and Δz chosen as 1 m.

3. The $M^{r,1}$ are summed from station 1 seaward and then interpolated linearly between stations to form total transports as continuous functions of x and T. These then are read off at the fixed station positions forming the corners of the box of interest, and subtracted to yield the total transport entering that side of the box as a function of T. The transports normal to the alongshore box sides at the desired offshore positions along each line are obtained by linear interpolation of M^a to the fixed positions of the box corner and

4. For the desired t_i, the transports of appropriate subsequent sections along either line A or B are interpolated linearly in time according to the scheme in Figure A1 and added to those of the other line for that box and time to finally obtain $M_{i,j}(T)$. In the subsequent calculations only $M_{i,j}(T)$ in the T range of max $(T_{\min}) \leq T \leq \min\ (T_{\max})$ of all the observations involved in forming $M_{i,j}(T)$ will be considered.

More sophisticated schemes allowing sloping bottoms at the stations with L in (A2) as a function of z as well as other "reasonable" choices for the structure of u and v within the bottom five meters were also tried. As long as the conservative T range given above for $M_{i,j}$ was retained and the corner shoreward of station 1 avoided, these only affected the final results by up to 5%. The same holds for other vertical interpolation schemes including the semi-Hermite splines used in P1.

The term $(V_{i+1,j} - V_{i-1,j})\ (t_{i+1} - t_{i-1})^{-1}$ is calculated for each t_i as follows:

1. the depths to isotherms in steps of .1°C as above from the profile observations are interpolated along each line to obtain isotherm depths at the fixed station

positions. These are then averaged over the stations in each line included in the box of interest. These averages are then interpolated in time and averaged over the two lines according to the scheme in Figure A1 to obtain $\hat{D}_{i,j}(T)$, the mean depth to isothermal surfaces for time t_i and box j. From echo soundings obtained during the study period along both lines and a line between them, bottom depths were plotted for the region between line A and B as shown in Figure 1. From these, area $C_j(z)$ could be calculated for every box j. Then

$$V_{i,j}(T) = \sum_{z_{\max}}^{\hat{D}_{i,j}(T)} C_j(z)\,\Delta z \tag{A3}$$

where $z_{\max}$ is the maximum depth in the box and (A3) is valid up to $T \leq \min(T_{\max})$ for all stations included in the box. If, in addition, we choose $T \geq \max(T_{\min})$ for all stations included in box j, then the isothermal surfaces do not intersect the bottom in the box and we have simply

$$(V_{i+1,j} - V_{i-1,j})(t_{i+1} - t_{i-1})^{-1} = (t_{i+1} - t_{i-1})^{-1}\,(\hat{D}_{i+1} - \hat{D}_{i-1})(C_j(0)) \tag{A4}$$

where $C_j(0)$ is the (constant) surface area of the box. Here as above with $M_{i,j}$ we will work in the range $\max(T_{\min}) \leq T \leq \min(T_{\max})$. Earlier attempts to extend this range to both higher and lower temperatures in order to cover a larger part of the thermocline showed that the results depended too heavily on assumptions like $C_j(D_{i,j}(T)) \sim C_{i,j}(\phi(T))$. In the T range we have chosen this holds almost identically.

From the above results and (3) we have

$$(w_D)_{i,j} = G_{i,j}(C_{i,j})^{-1} = G_{i,j}(C_j(0))^{-1}. \tag{A5}$$

From (1), (2) and (4) we have

$$f_{i,j} = F_{i,j}(C_j(0))^{-1} = c_p(C_j(0))^{-1} \int_{T_0}^{T} G_{i,j}\,dT' \tag{A6}$$

and finally from (5) we have

$$K_{i,j} = [(\partial T/\partial z)_{i,j}\, C_j(0)]^{-1} f_{i,j} \tag{A7}$$

where

$$(\partial T/\partial z)_{i,j} = [T(\overline{D}_{i,j} - \Delta z) - T(\overline{D}_{i,j} + \Delta z)]\,(2\Delta z)^{-1} \tag{A8}$$

and Δz is chosen to be 2.5 m. One sided differences are used at the top and bottom of the T range. Clearly uncertainties are introduced in $K_{i,j}$ if the actual $\partial T/\partial z$ varies significantly over the box at time t_i. However $\partial T/\partial z$ was found to be quite constant over the box and time of interest since vertical temperature gradients on constant T surfaces are considered and our T range was always well away from the mixed layers.

The calculation of w_{AD} in part 3 follows the same interpolation to fixed station positions and the same time interpolation scheme as used above but applied to individual stations not boxes.

(7) can be expressed

$$\begin{aligned}(w_{AD})_{i,j} = {} & D_{i+1,j} - D_{i-1,j}\,(t_{i+1} - t_{i-1})^{-1} \\ & + u_{i,j}\,(D_{j+1} - D_{j-1})_i\,(x_{j+1} - x_{j-1})^{-1} \\ & + v_{i,j}\,[(D_A)_i - (D_B)_{i,]_j}\,(62\text{ km})^{-1}.\end{aligned} \tag{A9}$$

All the results above were calculated in T space with increments of .1°C. They were then averaged over the following T intervals – $\leq$14.4, 14.4–14.7, 14.7–15.2, 15.2–15.8, $\geq$15.8. Averaging over several somewhat overlapping intervals was again chosen to increase the accuracy of the results while retaining sufficient structure. The choice of these specific intervals was guided by the wish to compare with gradient Richardson number results for which this interval choice appeared to represent an optimal trade off between resolution and accuracy.

Several properties of the results are of interest. M generally dominated over the $\partial V/\partial t$ term even on the daily time scale. M was usually dominated by contributions from the cross-shelf flow (i.e., across the alongshore sides): The alongshore transport entering the boxes at line A tended to leave them at line B. Daily values of w_{AD} were dominated by the $u\ \partial D/\partial X$ term over the outer part of the lines where onshore flow coincides with sloping isotherms and by this term and the $\partial D/\partial T$ term adjacent to the coast.

APPENDIX 2

Error analysis

The most obvious source of error in the NCCM calculations of $\overline{w}_D$, $\bar{f}$ and $\overline{K}$ is insufficient resolution in time and space for determining M. With our time resolution of ~2–4 days, significant aliasing of the results would be expected if there existed large amplitude motions with periods less than ~4 days in the study region during the study period. Although we have little data to look at this, some inferences can be made from the analysis of data from three recording current meters which were moored at station P (Fig. 1) at 37, 56 and 96 depths between 13 March and 19 May 1977 as part of the USA-Peru Joint II study. (The data was kindly supplied to me by Dr. R. L. Smith.)

The data was high-passed filtered to retain 99% of the energy at 74 hours, the local inertial period and subsequently analyzed with Rotary EOF analysis (Denbo and Allen, 1984). The only organized motion with amplitudes >.5 cm s^{-1} was found at the M_2 tidal and inertial frequencies. The M_2 results showed an almost purely barotropic, first REOF mode with 97.2%(+) and 95.8%(−) of the total variance. The first mode ellipses had a major axis orientation of 356° and amplitude of 3.2 cm s^{-1}. The major/minor axis ratio was 0.088; i.e., the tidal current is essentially alternating.

Table A1. A comparison of mean coefficients of turbulent heat diffusion based on the tidal "corrected" current meter data (see text) with those from the "uncorrected" data (in parentheses). Units are $cm^2 s^{-1}$.

T			Box		
(°C)	7-5	6-4	5-3	4-2	3-1
>15.8	−1.5(1.3)	5.6(7.0)	8.4(8.6)	8.3(8.1)	3.7(3.3)
15.2–15.8	−2.0(0.6)	4.5(5.8)	6.7(6.8)	5.6(5.4)	2.9(2.6)
14.7–15.2	−2.7(−.4)	2.9(4.0)	4.2(4.1)	3.0(3.0)	1.4(1.3)
14.4–14.7	−2.2(−.8)	1.3(1.9)	2.2(2.0)	—	—
<14.4	−0.9(−.3)	0.1(0.5)	—	—	—

Inertial period motion was dominated by + (anti clockwise) rotation with amplitude ~ 1.5 cm s^{-1}. These results suggest that the tidal current at each RCM depth z_i can be approximated well by an alternating current vector with amplitude W_i and orientation θ_i where

$$W_i = [\alpha_{1,i} + \alpha_{2,i} \sin (2\pi\tau_2^{-1}t + \beta_{2,i})] \sin (2\pi\tau_1^{-1}t + \beta_{1,i}). \tag{A10}$$

Here τ_1 is the M_2 period, 12.4206 hours and τ_2 is one half synodic month, 177.18 hours. The above relation explained the largest part of the variance (~70%) in the high-passed RCM records for $\theta_1 = 359°$, $\theta_{2,3} = 345°$ and the following amplitudes and phases $\alpha_{11} = \alpha_{12} = \alpha_{13} = 3.2$ cm s^{-1}, $\alpha_{21} = \alpha_{22} = \alpha_{23} = 1.1$ cm s^{-1}, $\beta_{11} = 157°$, $\beta_{12} = \beta_{13} = 164°$ and $\beta_{21} = \beta_{22} = \beta_{23} = 5°$ where the phases were referred to $t = 0$ at 13 March 1977, 1900 GMT.

Since tidal periods are fixed, I "corrected" our profiling observations for tidal aliasing by stepping the above empirical model forward in time into the study period and subtracting the tidal vector calculated for the time each profile was made from the observed current vectors. Linear interpolation of the tidal vectors was made between the depths of the RCM's and the values for $z = 37$ m and $z = 96$ m were used above and below these depths respectively. No attempt was made to model seaward and alongshore variations of the tidal current. In Table A1, the NCCM $\overline{K}$'s obtained from the new data set after "correction" for tidal aliasing are compared to the NCCM $\overline{K}$'s presented earlier from the original data set. This "correction" did not appear to affect $\overline{K}$ very much except to increase the negative values in box 7-5 somewhat. σ_K (not shown) only decreased slightly nearshore but increased by about 20% from already large values in box 7-5.

"Corrected" $\overline{K}$ were also calculated with $\theta_1 = 341°$ and $\theta_{2,3} = 327°$. This choice was motivated by local bottom topography orientation change between point P and our study area. The values of $\overline{K}$ (not shown) were even less affected in this case and a reduction of σ_K was found in box 7-5 accompanied by an increase of similar magnitude at all the other boxes. Thus the main conclusion is that tidal aliasing was not responsible for the large observed variability in daily w_D, f and K.

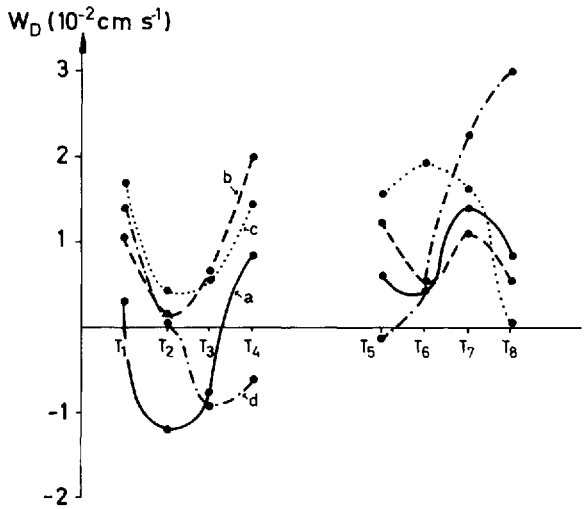

Figure A2. Time development of NCCM daily mean diapycnal vertical velocities for the T range 15.2–15.8 for boxes 7-5 (a), 6-4 (b), 4-2 (c) and 3-1 (d).

Figure A2 shows the time development of the daily values of w_D for boxes 7-5, 6-4, 4-2 and 3-1 and temperature range 15.2–15.8. Two effects can be seen which are responsible for much of the variability observed. The time developments for boxes 4-2 and 3-1 are negatively correlated; i.e., "excessive" inflow to one corresponds to "deficient" inflow to the other (since M was found to dominate $\partial V/\partial t$). This is indicative of a structure on the horizontal scale of box separation or less which could not be resolved. Clearly here the accuracy of the results would be improved by forming means over the two boxes. The large perturbation shown here and in Figure 3 during the first half of the study period has, however, at least the scale of the study area and an apparent time scale of several days. Since the results of conservation methods involve integration of currents from the bottom up to a surface of interest they are particularly sensitive to barotropic fluctuations. However σ_{w_D} (Fig. 2b) as well as σ_f and σ_K (Figs. 5b and 6b) for box 7-5 exhibited a larger increase toward the surface than could be explained by only barotropic aliasing.

Differences of fluxes across the alongshore sides of the boxes were found to make the largest contributions to M. The fluxes across each of these sides was based on data with ~60 km alongshore separation. Kundu and Allen (1976) found typical alongshore correlation scales of cross-shelf currents of only ~20–30 km off Oregon and attributed this result to a relatively large turbulence signal in the cross-shelf current. Indeed results from other investigations off Oregon (eg., Bryden *et al.*, 1980) support the existence of vigorous baroclinic eddying there. The internal Rossby radius over the wide shelf off northern Peru is about twice that off Oregon (P1, Smith, 1981) and alongshore correlation scales for baroclinic eddying may be expected to increase

correspondingly, perhaps approaching our 60 km separation scale. Shoreward fluxes at line A and B do not appear uncorrelated (P1, Fig. 6c) and, indeed, appear to be related to the local wind. Most other coastal upwelling investigations have shown high correlation of low passed cross-shelf currents with the local wind which generally has alongshore scales $\gg$60 km (eg., Smith, 1981). Furthermore, our alongshore separation appears sufficient to resolve structure which may be associated with local alongshore variations in bottom topography (with reservation for the station pairs nearest to the coast (Fig. 1)). Baroclinic eddying may indeed be responsible for most of the error in our NCCM calculations but the major problem appears to be aliasing in time.

A reviewer has suggested that actual volume changes within the boxes, i.e. due to "bulging" of isotherms, may lead to "extremely serious" problems for estimating the volume balances and w_D. From equations (1), (3) and (A4) the error in $w_D(T)$ due to this effect can be estimated by $\Delta D'(T)\tau^{-1}$ where τ is the integration time for each calculation and $\Delta D' = D'_{t+\tau} - D'_t$ where $D' \equiv \bar{D} - D$, the difference between the real and estimated (Appendix 1) mean depth to the isotherm T within a box. Note that for stationary "bulging," $D'_{t+\tau} \sim D'_t$ and $\Delta D' \sim 0$. Earlier results showed that depths to isotherms were quite constant in the outer half of both lines A and B during the study period and that variations of the thermal field in the inner half of lines A and B were very well correlated (P1, Figs. 3c, d and Fig. 6a). It would be hard to reconcile these results with a $\Delta D'$ greater than about 5 m. With $\tau = 2$ days, this $\Delta D'$ would imply an error in w_D of $\sim 3 \times 10^{-3}$ cm s^{-1} and this effect may indeed account for some of the error in the daily estimates of w_D and k (Fig. 3). However $\tau = 10$ days for the mean NCCM w_D and k,—the important results of this calculation—and an insignificant error of $\sim .6 \times 10^{-3}$ cm s^{-1} follows.

Instrumentation error is a certain source of error in all the results presented above. While the accuracy and precision of the temperature-depth sonde were sufficient to avoid significant errors here, the pendulum current meters used have uncertainties of ± 2 cm in speed and $\pm 5°$ in direction according to our calibrations. The way the profiling system is used suggests that systematic errors are avoided (P1)—the gelatin compartments are drawn at random out of a pot of hot water and the plastic vanes likewise out of a box on deck. It then was natural to study the errors introduced by the current meter inaccuracies in a Monte Carlo simulation. A random number generator was chosen with a normal distribution adjusted such that 90% probability was bounded by ± 2 cm s^{-1} for current and $\pm 5°$ for direction. A random current vector formed in this way was added to each observed one for the whole data set (about 1000 measurements). This was repeated 100 times to form 100 new, randomly perturbed data sets and NCCM $\overline{w}_D$, $\bar{f}$, $\bar{K}$ as well as $\overline{Ri}$ were calculated from the new data sets as above. Ends of a central 90% confidence interval were defined by the sixth and ninety-fourth value, ordered by magnitude, of the variable of interest.

The NCCM results were quite robust to these random perturbations. The $\overline{w}_D$, $\bar{f}$ and $\bar{K}$ were all within 7% of their original values at the 90% confidence levels. This is not

surprising since these are based on vertical integration of currents in which the random contributions would tend to cancel. It is a firm conclusion that instrumental errors were not significant for NCCM results.

The situation is different for the Richardson numbers. Table A2 shows the range $\overline{Ri}_6 - \overline{Ri}_{94}$, taken as a central 90% confidence interval. The 90% confidence interval varies from about ±5% to ±12% $\overline{Ri}$ reflecting the same structure as $\overline{Ri}_{\min}$ and $\overline{Ri}_{\max}$ earlier. More important however is the bias demonstrated by the shift of the range $\overline{Ri}_6 - \overline{Ri}_{94}$ with respect to $\overline{Ri}$ toward smaller values. Indeed the larger $\overline{Ri}$ fall outside this range. This bias is due to the nonlinearity in the definition of Ri: S^2 will always tend to be increased by random perturbations. This can be seen from $[(x + \delta)^2 + (x - \delta)^2]/2 = x^2 + \delta^2$ where $\pm\delta$ are equally-likely random perturbations. The approximate dependency of the bias on Ri can be shown as follows

$$\text{Bias} \equiv \overline{N}^2/\overline{S}^2 - \overline{N}^2/(\overline{S}^2 + \delta^2) = (\delta^2/\overline{S}^2)\,(\overline{Ri}) \sim \delta^2/\overline{N}^2(\overline{Ri})^2 \qquad \text{(A11)}$$

for $\overline{N}^2$ nearly constant as holds for the x,T bins we consider and $\delta^2 \ll S^2$ which we also found to be true. Here bias is estimated by $\overline{Ri} - \overline{Ri}_{50}$ listed in Table A2. The $\overline{Ri}^2$ dependency derived above proves to describe this estimate well.

Whereas the bias calculated above results from perturbating the measured current vector, one should think of the measured current vectors as randomly-perturbed (due to randomly-distributed instrumental error) real current shears. This implies that the real current shears were associated with larger mean Richardson numbers than our calculated Ri. Based on the above results, best estimates for bias-corrected mean Richardson numbers, $\overline{Ri}^*$, would be

$$\overline{Ri}^* \sim \overline{Ri} + \overline{Ri}^2\,(\overline{Ri} - \overline{Ri}_{50})/\overline{Ri}_{50}^2.$$

These are listed in Table A2 together with bias-corrected $\overline{Ri}_{\min}$ and $\overline{Ri}_{\max}$. The effect of random instrument error on the other Ri results presented in part 4b was also investigated. The frequency distributions (Fig. 7) were found to be shifted only slightly in the manner to be expected from the above results. Mean Ri calculated from the whole data set was virtually unaffected, 0.265 and 0.270 before and after the bias correction, since mean Ri is dominated by large $S^2 \gg \delta^2$. Likewise the % $Ri \leq 0.25$ statistic was only slightly changed by random instrument errors. Central 90% confidence intervals calculated as above from the 100 Monte Carlo simulations are given in Figure 3c.

Another source of error in Ri is our choice of salinity distribution based on observations in the study area made in Nov. 1977 before our study (Herman, 1982; Doe, 1978). All observations from the study area in these references showed a slight salinity maximum centered ~16°C between 35.050 and 35.100 in the offshore part of the section, but tending to weaken toward shore, as well as linear T-S curves below and directly above it. I estimate the possible error in Ri of Figure 8 and Table 3 due to uncertainty in the actual salinity distribution to be ±10%.

Table A2. Stationwise, mean Richardson numbers, their 90% central confidence intervals ($\overline{Ri}_6$–$\overline{Ri}_{94}$), bias ($\overline{Ri}$–$\overline{Ri}_{50}$), and bias-corrected mean, minimum, and maximum Richardson numbers. ($\overline{Ri}^*$, $\overline{Ri}^*_{min}$ and $\overline{Ri}^*_{max}$).

Box	$\overline{Ri}$	$\overline{Ri}_6$–$\overline{Ri}_{94}$	$\overline{Ri}$–$\overline{Ri}_{50}$	$\overline{Ri}^*$	$\overline{Ri}^*_{min}$	$\overline{Ri}^*_{max}$
3-1	.192	.176–.207	.002	.194	.115	.343
	.260	.240–.273	.003	.263	.173	.457
	.221	.201–.226	.008	.229	.165	.324
4-2	.182	.159–.185	.012	.195	.112	.389
	.213	.119–.221	.003	.215	.152	.302
	.316	.290–.326	.008	.323	.229	.500
	.269	.243–.277	.012	.282	.182	.506
	.225	.193–.232	.014	.242	.154	.442
5-3	.216	.201–.227	.002	.218	.164	.296
	.338	.307–.352	.011	.350	.270	.486
	.314	.275–.322	.016	.331	.234	.591
	.289	.248–.305	.014	.304	.212	.487
6-4	.408	.296–.417	.063	.497	.283	1.180
	.263	.243–.276	.004	.266	.199	.364
	.279	.251–.293	.010	.289	.209	.415
	.325	.282–.326	.019	.347	.255	.511
	.469	.374–.484	.053	.536	.388	.773
7-5	.577	.396–.574	.111	.746	.509	1.165
	.344	.323–.354	.007	.350	.253	.505
	.304	.270–.310	.015	.320	.223	.491
	.362	.307–.358	.030	.398	.309	.538
	.645	.489–.597	.105	.794	.646	1.002
	.568	.413–.554	.091	.697	.437	1.247

In the light of the size of the errors estimated above the real question with respect to $\overline{Ri}$ is do they give a representative distribution in x and T for the quite strong, shear-driven turbulence which seemed to exist over the wide shelf off northern Peru during November–December 1977. The good correspondence between the distributions in Figures 8 and 9 suggest that they are representative with reservation for the Ri in the lower layers nearshore. The strong but well organized time variation of daily Ri (Fig. 3c) suggest that $\overline{Ri}$ will depend upon the averaging interval but also that the moderate wind event was resolved well. A (re)visit to the study area with a modern Ri-profiler would be well motivated (and indeed is planned).

REFERENCES

Allen, J. S. 1973. Upwelling and coastal jets in a continuously stratified fluid. J. Phys. Oceanogr., *3,* 245–257.

Barton, E. D., A. Huyer and R. L. Smith. 1977. Temporal variation observed in the hydrographic regime near Cabo Corveiro in the northwest African upwelling region, February to April 1974. Deep-Sea Res., *24,* 7–23.

Brink, K. H., D. Halpern and R. L. Smith. 1980. Circulation in the Peruvian upwelling system near 15S. J. Geophys. Res., *85,* 4036–4048.

Bryden, H. L., D. Halpern and R. D. Pillsbury. 1980. Importance of eddy heat flux in a heat budget for Oregon coastal waters. J. Geophys. Res., *85,* 6649–6653.

Crawford, W. R. 1982. Pacific equatorial turbulence. J. Phys. Oceanogr., *12,* 1137–1149.

Csanady, G. T. 1976. Topographic waves in Lake Ontario. J. Phys. Oceanogr., *6,* 93–103.

Denbo, D. W. and J. S. Allen. 1984. Rotary empirical orthogonal function analysis of currents near the Oregon coast. J. Phys. Oceanogr., *14,* 35–46.

De Szoeke, R. A. and J. G. Richman. 1984. On wind-driven mixed layers with strong horizontal gradients—A theory with application to coastal upwelling. J. Phys. Oceanogr., *14,* 364–377.

Doe, L. A. E. 1978. Project Icane, Bedford Inst. of Oceanogr. Report B1-R-78-6, 211 pp.

Ellison, T. H. 1957. Turbulent transport of heat and momentum from an infinite rough plane. J. Fluid. Mech., *2,* 456–466.

Ellison, T. H. and J. S. Turner. 1960. Mixing of dense fluid in a turbulent pipe flow. J. Fluid. Mech., *8,* 423–448.

Endoh, M., C. N. K. Mooers and W. R. Johnson. 1981. A coastal upwelling circulation model with eddy viscosity depending on Richardson number, *in* Coastal Upwelling, F. A. Richards, ed., American Geophysical Union, 203–208.

Fjeldstad, J. E. 1944. Internal Waves of Tidal origin. Geofys. Publr. 25,5.

Foo, E. 1981. A two-dimensional diabatic isopycnal model—Simulating the coastal upwelling front. J. Phys. Oceanogr., *11,* 604–626.

Gill, A. E. and A. J. Clarke. 1974. Wind induced upwelling, coastal current and sea level changes. Deep-Sea Res., *21,* 325–345.

Herman, A. W. 1982. Spatial and temporal variability of chlorophyll distributions and geostrophic current estimates on the Peru Shelf at 9S. J. Mar. Res., *40,* 185–207.

Hsieh, W. W. 1982. On the detection of continental shelf waves. J. Phys. Oceanogr., *12,* 414–427.

Johnson, W. R., J. C. Van Leer and C. N. K. Mooers. 1976. A cyclesonde view of coastal upwelling. J. Phys. Oceanogr., *6,* 566–574.

Kundu, P. K. 1984. Numerical calculations of coastal flow with turbulent dynamics. Deep-Sea Res., *31,* 39–60.

Kundu, P. K. and J. S. Allen. 1976. Some three-dimensional characteristics of low frequency current fluctuations near the Oregon coast. J. Phys. Oceanogr., *6,* 181–199.

Kundu, P. K., J. S. Allen and R. L. Smith. 1975. Model decomposition of the velocity field near the Oregon coast. J. Phys. Oceanogr., *5,* 683–704.

Martinsen, E. A. and J. E. Weber. 1981. Frictional influence on internal Kelvin waves. Tellus, *33,* 402–410.

McCreary, J. 1981. A linear stratified ocean model of the equatorial undercurrent. Phil. Trans. Roy. Soc. London, *298,* 603–625.

McCreary, J. and S. Chao. 1985. Three-dimensional shelf circulation along an eastern ocean boundary. J. Mar. Res., *43,* 13–36.

Mooers, C. N. K., C. A. Collins and R. L. Smith. 1976. The dynamic structure of the frontal zone in the coastal upwelling region off Oregon. J. Phys. Oceanogr., *6,* 3–21.

Munk, W. H. and E. R. Anderson. 1948. A note on the theory of the thermocline. J. Mar. Res., *7,* 276–295.

Mysak, L. A. 1980. Topographically trapped waves. Ann. Rev. Fluid. Mech., *12,* 45–76.

Osborn, T. R. 1980. Estimates of the local rate of vertical diffusion from dissipation measurements. J. Phys. Oceanogr., *10,* 83–89.

Ozmidov, R. V. 1965. On the turbulent exchange in a stably stratified ocean. Atmos. Ocean. Phys., *8,* 853–860.

Pacanowski, R. C. and S. G. H. Philander. 1981. Parameterization of vertical mixing in numerical models of tropical oceans. J. Phys. Oceanogr., *11,* 1443–1451.

Pedlosky, J. 1978. A nonlinear model of the onset of upwelling. J. Phys. Oceanogr., *8,* 178–187.
Shaffer, G. 1979. Conservation calculations in natural coordinates (with an example from the Baltic). J. Phys. Oceanogr., *9,* 847–855.
—— 1982. On the upwelling circulation over the wide shelf off Peru: 1. Circulation. J. Mar. Res., *40,* 293–314.
Shaffer, G. and L. Djurfeldt. 1983. On the low-frequency fluctuations in the Eastern Skagerrak and in Gullmaren. J. Phys. Oceanogr., *13,* 1321–1340.
Shaffer, G. and U. Rönner. 1984. Denitrification in the Baltic proper deep water. Deep-Sea Res., *31,* 197–202.
Smith, R. L. 1968. Upwelling. Oceanogr. Mar. Biol. Ann. Rev., *6,* 11–46.
—— 1974. A description of current, wind and sea-level variations during coastal upwelling off the Oregon coast, July–August 1972. J. Geophys. Res., *79,* 435–443.
—— 1978. Poleward propagating perturbations in currents and sea levels along the Peru coast. J. Geophys. Res., *83,* 6083–6092.
—— 1981. A comparison of the structure and variability of the flow field in three coastal upwelling regions: Oregon, Northwest Africa and Peru, *in* Coastal Upwelling, F. A. Richards, ed., American Geophysical Union, 107–118.
Suginohara, N. and Y. Kitamura. 1984. Long-term coastal upwelling over continental shelf-slope. J. Phys. Oceanogr., *14,* 1095–1104.
Thorpe, S. A. 1973. Experiments on instability and turbulence in a stratified shear flow. J. Fluid. Mech., *61,* 731–751.
—— 1977. Turbulence and mixing in a Scottish loch. Philos. Trans. Roy. Soc. London Ser. A, *286,* 125–181.
Turner, J. S. 1973. Buoyancy Effects in Fluids. Cambridge University Press.
Walin, G. 1977. A theoretical framework for the description of estuaries. Tellus, *29,* 128–136.
Wang, D.-P. and C. N. K. Mooers. 1977. Evidence for interior dissipation and mixing during a coastal upwelling event off Oregon. J. Mar. Res., *35,* 697–713.
Wyrtki, K. 1966. Oceanography of the eastern equatorial Pacific Ocean. Oceanogr. Mar. Biol. Ann. Rev., *4,* 33–68.

Received: *17 July, 1985;* revised: *21 March, 1986.*